ChemNanoMat

CHEMNANOMAT
CHEMISTRY OF NANOMATERIALS FOR ENERGY, BIOLOGY AND MORE

ACES Asian Chemical Editorial Society

RESEARCH ARTICLE OPEN ACCESS

Machine Learning-Assisted Fabrication of 3D-Printed Extracellular Matrix Models

Maddalena Bracchi[1] | Francesco Nicotra[1] | Laura Russo[1,2,3]

[1]School of Medicine and Surgery, Università degli Studi di Milano-Bicocca, Monza, Italy | [2]Fondazione IRCCS San Gerardo dei Tintori, Monza, Italy | [3]CURAM Research Ireland Centre for Medical Devices, University of Galway, Galway, Ireland

Correspondence: Laura Russo (laura.russo@unimib.it)

Received: 28 November 2025 | **Revised:** 4 May 2026 | **Accepted:** 13 May 2026

Keywords: 3D printing | AI | ECM mimics | hydrogel | machine learning

ABSTRACT

Mimicking the extracellular matrix (ECM) is challenging due to the complex composition, architecture, morphology, and mechanical properties of native tissues, which are key targets in tissue engineering. 3D printing enables the fabrication of ECM models with high spatial resolution exploiting hydrogels retaining essential viscoelastic and water retention properties for cell survival. In this study, a machine learning (ML)-assisted approach was developed to describe the printing behavior of hydrogels, demonstrating the potential to predict printability, despite the limitations imposed by the small available dataset. To generate the hydrogels, gelatin and hyaluronic acid were functionalized with γ-thiobutyrolactone and cysteamine, respectively. Crosslinking was carried out via thiol–ene photochemical reaction with 4-arm-PEG functionalized with norbornene. The resulting formulations were assessed via swelling tests to evaluate their stability, and the most promising candidates were further characterized chemically, morphologically, and rheologically. Cytocompatibility was validated through viability assays using human bone marrow-derived mesenchymal stem cells. High-resolution 3D printing via stereolithography was performed to confirm the printability of the selected hydrogels. Based on these results, a preliminary predictive ML model was developed to estimate and predict hydrogel printability.

1 | Introduction

Reproducing the native extracellular matrix (ECM) composition, architecture, and stiffness is crucial in tissue engineering [1, 2]. These features regulate key cellular processes fundamental in directing cell behavior such as focal adhesion, cytoskeletal organization, cell spreading, and lineage specification [3–5]. Hydrogels are increasingly used in tissue engineering due to their structural and compositional similarity to the ECM, providing a supportive environment for cell survival and proliferation [6, 7]. They are three-dimensional networks of crosslinked hydrophilic polymers, with swelling capacity determined by functional groups such as -NH_2, -COOH, -OH, -$CONH_2$, -CONH, and -SO_3H [8]. The combination of hydrophilic polymers composition and crosslinking conditions (time, temperature, pH) determines the rheological and mechanical properties of hydrogels, which are critical for reproducing native tissue stiffness [9, 10]. Furthermore, 3D printing provides precise control over hydrogel architecture, allowing closer replication of tissue microstructures [11]. Factors such as stiffness, porosity, and crosslinking density govern the structural stability of printed constructs, influencing their potential applications [12–14]. Beyond extrusion-based methods, stereolithography has emerged as a powerful approach for 3D printing hydrogels [15, 16]. This technique relies on light-induced crosslinking to achieve high spatial resolution and complex geometries with smooth surfaces [17–19]. The main challenge lies in designing hydrogel formulations that combine sufficient photoreactivity for rapid curing with mechanical and structural properties suitable for the intended application [20].

The thiol–ene reaction is classified as a "click" chemistry because it proceeds under mild conditions (aqueous solutions, physiological temperature, and pH), without producing byproducts, and is rapid, spontaneous, and highly selective [21–23]. Unlike many other "click" reactions, thiol–ene is light-initiated, providing excellent spatial control [24–26]. Specifically, under the action of light or thermal initiators, thiol groups react with alkenes to form thioether bonds. In this context, the very fast thiol–norbornene photoclick reaction has been widely exploited for tissue engineering applications [27].

Advances in computational simulation, together with the need to develop materials capable of replicating the complexity of native tissues, have enabled the use of machine learning (ML) and deep learning approaches to accelerate materials development while reducing time and cost [28–31]. In the study by Sarah et al., predictive ML models were developed for shear-thinning, extrusion-based 3D printable hydrogels using rheological data from alginate, gelatin, and TEMPO-nanofibrillated cellulose systems across a range of shear rates. The model enabled efficient optimization of hydrogel formulations, reducing the need for extensive experiments [32]. In this context, ML techniques can be particularly useful for predicting the printability of hydrogels, by incorporating parameters that are critical for guiding 3D printing processes, especially those initiated by light [33, 34]. In Ruberu et al., ML was exploited to optimize 3D bioprinting of GelMA and HAMA hydrogels by evaluating the filament formation of the bioink and the layer stacking of the 3D scaffold to find the optimal printing parameters [35]. While ML is widely used to optimize extrusion-based 3D printing of hydrogels, its application in stereolithography remains limited and underexplored. This work therefore proposes a predictive framework for photocrosslinkable systems.

In this study, thiol–norbornene crosslinking was explored to develop gelatin and hyaluronic acid-based hydrogels for the fabrication of high-resolution 3D-printed scaffolds for tissue engineering. This method uses a light-initiated reaction between thiol and alkene groups, forming stable thioether bonds [36]. Gelatin was selected because it is derived from collagen, a key ECM protein, and offers several advantages such as biocompatibility, biodegradability, low immunogenicity, and Arg-Gly-Asp (RGD) sequences that enhance cell adhesion. Hyaluronic acid is a non-sulfated glycosaminoglycan that plays a crucial role in tissue hydration and homeostasis, while also modulating inflammatory responses. Its viscoelastic and water-retaining properties in aqueous environments make it particularly valuable for tissue engineering applications [37–41].

After introducing thiol groups to gelatin and hyaluronic acid, crosslinking was carried out with commercially available 4-arm-PEG functionalized with norbornene (PEG-NB), generating various formulations by adjusting the concentrations of the components. These hydrogels were then characterized chemically, physically, and mechanically to identify the most suitable candidates for 3D printing. Selected formulations were subsequently printed and subjected to biological evaluation. Finally, a preliminary predictive model was developed to estimate and predict hydrogel printability, and its performance was validated by printing additional formulations and comparing the experimental outcomes with the computational predictions.

2 | Materials and Methods

2.1 | Materials

Gelatin from porcine skin (gel strength 300, Type A), γ-thiobutyrolactone 98%, N-hydroxysuccinimide (98%, NHS), cysteamine 95%, sodium bicarbonate (98%, $NaHCO_3$), sodium hydroxide (97%, NaOH), DL-Dithiothreitol (99%, DTT), MES hydrate (≥99.5%), dialysis tubing cellulose membrane (MWCO 14 kDa), Lithium phenyl-2,4,6 trimethylbenzoylphosphinate (95%, LAP), 5,5′-Dithiobis(2-nitrobenzoic acid) (DTNB), L-cysteine, sodium azide (≥99.5%), deuterium oxide (99.9 atom %D, D_2O, 0.05 wt.% 3-(trimethylsilyl)propionic-2,2,3,3-d4 acid, sodium salt, TMSP), and Tartrazine (dye content, ≥85%) were purchased from Merck (Milan, Italy). Hyaluronic acid sodium salt with an average molecular weight of 1.0–2.0 million Da was purchased from Carbosynth (Switzerland). Dulbecco's phosphate-buffered saline (DPBS) was purchased from Euroclone S.p.A. (Milan, Italy). 1-(3-Dimethylaminopropyl)-3-ethylcarbodiimide (>98% purity, EDC) was purchased from TCI Chemicals Europe (Belgium). 4-arm-PEG-norbornene (PEG-NB) MW 10k was purchased from Divbio Science Italia (Brenzone, Italy). For cell experiments, human bone marrow-derived mesenchymal stem cells (hBM-MSCs), mesenchymal stem cell basal medium, and mesenchymal stem cell growth kit for bone marrow-derived MSCs (recombinant human Fibroblast growth factor basic, rh FGF-b, recombinant human Insulin-like growth factor 1, rh IGF-1, L-Alanyl-L-Glutamine) were purchased from LGC Standards (Milan, Italy). Fetal bovine serum (FBS), trypsin-EDTA solution (0.5 g porcine trypsin and 0.2 g EDTA), and Penicillin-Streptomycin (P/S, 10,000 units penicillin and 10 mg streptomycin/mL) were purchased from Merck (Milan, Italy). Amphotericin B (AMP), Alamar blue cell viability reagent, LIVE/DEAD for mammalian cells, superfrost plus adhesion microscope slides, Fluoromount-G mounting medium, and Alexa fluor 633 phalloidin were purchased from Thermo Fisher Scientific (Monza, Italy).

2.2 | ^{1}H-NMR Analysis

^{1}H-NMR spectra were obtained using a Varian Mercury 400 MHz, with samples prepared by dissolving 5 mg of the product in 500 μL of D_2O. For hyaluronic acid functionalized with thiol (HA-SH), the degree of functionalization (DoF), defined as the ratio between thiol groups and the total weight of the product, was determined by comparing the ratio of the integrals of the peaks of the protons adjacent to -SH groups and the TMSP reference peak integral (Equation (1)). For gelatin functionalized with thiol (Gel-SH), it was not possible to isolate the thiol groups in the spectrum due to overlapping signals from Gel. Therefore, the decrease in the ε-methylene protons of the lysine side chain at 2.9 ppm was qualitatively assessed as an indicator of successful functionalization.

$$DoF\,[\%] = \frac{m\,\text{cysteamine}}{m\,\text{sample}} \cdot 100 \tag{1}$$

Equation 1. Formula to calculate DoF from HA-SH ^{1}H_NMR spectrum: Briefly, the number of moles of cysteamine was obtained using the integral calculated from ^{1}H-NMR. Then, the mass of cysteamine (m cysteamine) was calculated by multiplying the moles by the molecular weight of cysteamine

(77.15 g/mol). Finally, DoF was obtained, where m sample is the mass of the sample used in the test.

2.3 | Ellman's Assay

Ellman's assay is a colorogenic test used to quantify the concentration of thiol groups in Gel-SH and HA-SH. Initially, three different solutions were prepared as follows: the first one was composed by 1 mM EDTA in PBS pH 8, the second one 0.3 mg/mL DTNB in PBS pH 8, and the third one a 2 mg/mL sample solution in dH_2O, preparing a triplicate for each sample. Subsequently, 250 μL of sample solution was combined with 250 μL of first and 250 μL of second solutions and stirred at 1600 rpm for 30 min at room T. The blank was prepared in the same way, except for the third solution, substituted with 250 μL of dH_2O. Finally, solutions were transferred to a 96-well microplate (100 μL per well), and absorbance at 412 nm was measured using UV-Vis SPECTROstar Nano (BMG LABTECH, Offenburg, Germany). Each sample was analyzed in triplicate, and results were processed using the equation of the calibration curve, obtained with cysteine solution at different concentrations (1.4, 1.2, 1, 0.8, 0.6, 0.4, and 0.2 mM).

2.4 | Swelling Test

The equilibrium swelling ratio was evaluated at three different pH values. Briefly, hydrogels were formed into cylindrical molds with a diameter of 15 mm, 500 μL in triplicate for each formulation, and their initial weight (w0) was measured. Subsequently, they were incubated in PBS 5.5, 7.4, and 8.5 with 0.02% w/V sodium azide at 37°C, and their wet weight (wt) was obtained at different time points (t): 1, 2, 3, 4, 5h, and days 1, 3, 5, 7, 14, and 28. Finally, their swelling ratio $\Delta w(t)_{\%}$ was calculated using Equation (2).

$$\Delta w(t)_{\%} = \frac{w_t - w_0}{w_0} \cdot 100 \quad (2)$$

Equation 2. Formula to calculate swelling ratio ($\Delta w(t)_{\%}$)

2.5 | Rheological Characterization

Rheological characterization of hydrogels was performed with a Modular Compact Rheometer MCR-92 Anton Paar (Anton Paar Italy, Rivoli, Italy), equipped with a Peltier temperature control unit. A 50 mm stainless steel parallel plate was used, with a gap between the plates set at around 1000 μm; and the temperature was maintained at 40°C. Oscillatory amplitude strain sweep test was conducted to determine the elastic modulus (G'), the loss modulus (G''), the yield point (where G' and G'' are constant) and the flow point (crossover of G' and G'') by applying a strain sweep range from 0.1% to 1000% at an angular frequency of 10 s^{-1}.

2.6 | Compression Test

Mechanical properties of formulations were investigated with Texture Analyzer (Stable Micro Systems, Godalming, United Kingdom) equipped with a 10 mm delrin cylindrical probe. Briefly, hydrogels were formed in 12-well plates, in triplicate for each formulation, and cut with a punch to obtain 10 mm diameter and 2 mm width cylinders. A compression test was conducted until 25% deformation with a 10-s hold and unload. The pre-test and post-test speeds were set at 600 mm/min, the test speed was 1.2 mm/min, and trigger force was 0.05 N. Some parameters were calculated, such as yield stress and strain (σ_y and ε_y, respectively), stress at 25% deformation (σ_{25}), and hysteresis area at $\varepsilon = 25\%$.

2.7 | SEM Analysis

Hydrogels were formed in 2 mL Eppendorf tubes as described below, frozen at −20°C overnight, and stored at −80°C until freeze-drying. Cross sections were obtained from lyophilized samples with a sharp blade, mounted on adhesive carbon black and sputter coated with gold (Sputter Coater S150B, Edwards Vacuum, Cinisello Balsamo, Italy). Images were acquired using electron microscope (Gemini SEM500, Zeiss, Milan, Italy) at 5 kV and 25 mm working distance.

2.8 | Indirect Cytotoxicity Test

Indirect cytotoxicity test was performed to verify the non-cytotoxicity of hydrogels since DTT was used, unless in small quantities, to optimize the crosslinking. First, LAP stock solution 0.1 M was prepared and filtered, while Gel-SH, HA-SH, and PEG-NB solutions were sterilized under biological hood using UV light for 30 min. DTT was added before sterilization. Then, 100 μL of hydrogel were formed in triplicate at specific time points (day 1, day 3, day 7) for each formulation, following the procedure described above, and left at 37°C for 30 min for stabilization. Subsequently, hydrogels were immersed in culture medium (mesenchymal stem cell basal medium with 7% FBS, 15 ng/mL Rh IGF-1, 125 pg/mL Rh FGF-b, 2.4 mM L-Alanyl-L-Glutamine, 1% P/S and 1% AMP) for 1, 3, and 7 days. Culture medium was used as control. hBM-MSCs were seeded at a density of 10 000 cells/well in a 96-well plate and incubated at 37°C with 5% CO_2. Eluates were then added to seeded cells, and after 24 h, an Alamar Blue assay was performed, measuring absorbance at 570 and 600 nm wavelengths (UV-Vis SPECTROstar Nano BMG LABTECH, Offenburg, Germany). Finally, percentage viability was calculated using Equation (3).

$$\text{Viability}\,[\%] = \frac{(E_{\text{OXI}}600 \cdot A570) - (E_{\text{OXI}}570 \cdot A600)}{(E_{\text{RED}}570 \cdot C600) - (E_{\text{RED}}600 \cdot C570)} \cdot 100 \quad (3)$$

Equation 3. Equation for cell viability, where $E_{\text{OXI}}550$ and $E_{\text{OXI}}600$ are the molar extinction coefficients of oxidized Alamar Blue reagent at 570 (80586) and 600 nm (117216), respectively, A570 and A600 are absorbances of test wells at 570 and 600 nm, respectively, $E_{\text{RED}}550$ and $E_{\text{RED}}600$ are the molar extinction coefficients of reduced Alamar Blue reagent at 570 (155677) and 600 nm (14652), and C570 and C600 are absorbances of negative control wells at 570 and 600 nm, respectively.

2.9 | Viability Test and Morphological Characterization of Cells

A viability test was performed under two different cell seeding conditions: on the surface and within the hydrogels. Hydrogels were prepared as previously described. For the condition with cells inside the hydrogels, cells were added to the formulation before UV crosslinking, whereas for surface seeding, cells were added after the UV crosslinking step. In both conditions, cell density was kept at 1×10^6 cells per sample, and cultures were maintained for 21 days. Alamar Blue assays were performed at designated time points (days 1, 3, 7, 10, 14, 17, and 21), measuring metabolic activity through absorbance. Absorbance values were also normalized to those at day 1 for each time point. Cells plated directly on the well bottom were used as the control group. Live-Dead staining was performed on days 7, 14, and 21 to qualitatively determine cell viability after printing and to compare the two seeding conditions. Additionally, viability was semi-quantitatively evaluated using Equation (4).

$$\text{Viability}\,[\%] = \frac{N_{\text{green}}}{N_{\text{green}} + N_{\text{red}}} \cdot 100 \tag{4}$$

Equation 4. Formula to calculate cell viability from a Live-Dead assay, where N_{green} and N_{red} represent the number of cells stained with green fluorescent calcein-AM to indicate intracellular esterase activity and red-fluorescent ethidium homodimer-1 to indicate loss of plasma membrane integrity [37].

Morphological characterization was assessed with Phalloidin-DAPI assay, in which nuclei were stained in blue and actin filaments in red. Briefly, samples cultured until day 21 were washed with DPBS, fixed in 10% formalin for 30 min, and then rewashed with DPBS. Hydrogels were then embedded in O.C.T. compound and frozen at −80°C. Samples were then sectioned with a cryostat (Leica CM 1520, Cornegliano Laudense, Lodi, Italy) to obtain 50 µm thick coronal sections and mounted on microscope slides. Hydrogel slides were subsequently incubated with 0.1% Triton X-100 in DPBS for 5 min for permeabilization, 20 nM Phalloidin for 30 min, and 1X DAPI for 10 min at room temperature, washed with DPBS, and mounted with Fluoromount-G medium. Roundness comparison was performed using Fiji ImageJ, where roundness is defined as Equation (5) [42]. Roundness assumes a value of 1 in the presence of an ideal circle, unless it is lower in other shapes.

$$R = \frac{4A}{\pi \cdot d_{max}^2} \tag{5}$$

Equation 5. Equation used to calculate roundness of cell nuclei, where A is the nucleus area and d_{max} is the maximum diameter of the nucleus

2.10 | 3D Printing Test

3D printing of hydrogels was performed with Lumen X LDP 3D printer (Cellink, Göteborg, Sweden) with a UV wavelength of 405 nm. Briefly, materials were prepared as previously described but 0.025% w/V Tartrazine was added before printing as photoabsorber to improve printing quality [43]. Printing parameters used were 15 s as the exposure time, 3X as the first layer time scale factor, and 90% as the projector power level. Printing was performed at room temperature, and two samples for each formulation were prepared. After printing, the samples were washed in PBS pH 7.4 until they became transparent and then observed using an inverted microscope (Zeiss Axio Observer/Cell Observer) in brightfield mode. Printing parameters were analyzed to assess the quality of the 3D-printed structures, with measurements obtained using Fiji ImageJ. The spreading ratio (SR), which reflects the shape fidelity of the printed structure, was calculated using Equation (6), whereas an ideal value is close to 1, indicating a good match between the actual and theoretical filament diameters [44, 45].

$$\text{Spreading ratio}\,(SR) = \frac{w_i}{w_0} \tag{6}$$

Equation 6. Formula used to calculate the spreading ratio, where w_i represents the measured width of the printed strand and w_0 represents the theoretical strand width. An SR value close to 1 indicates high shape fidelity of the printed structure.

Furthermore, printing accuracy (PA) and uniformity factor (UF) were calculated using Equations (7) and (8), respectively, based on measurements from the inner squares of the 3D-printed structures. A PA value close to 100% indicates strong agreement between the printed construct and the original 3D model design [46]. UF was used to evaluate how closely the printed pores matched the intended square geometry [45]. As reported in previous works, a UF value closer to 1 means well-defined square shapes, while $UF < 1$ correlates with rounded shapes and $UF > 1$ with rough pore sides [47, 48].

$$\text{Printing Accuracy}\,(PA)\,[\%] = \left[1 - \left(\frac{|A_i - A_0|}{A_0}\right)\right] \cdot 100 \tag{7}$$

Equation 7. Formula to calculate PA, where A_i and A_0 indicate the printed strand pore area and the theoretical square area, respectively.

$$\text{Uniformity Factor}\,(UF) = \frac{(pore\,\text{perimeter})^2}{16 \cdot pore\,area} \tag{8}$$

Equation 8. Formula to obtain uniformity factor (UF), where pore perimeter and pore area are measured on the squared 3D printed structures.

Ten measurements were taken for each parameter, and the mean values were used to calculate the three printing parameters. Printed samples were then put in PBS 7.4 with 0.02% w/V sodium azide at 4°C for 5 days, and the width increase (Δw_i) was then calculated using Equation (9).

$$\Delta w_i = \frac{w_{i\_day0}}{w_{i\_day5}} \tag{9}$$

Equation 9. Formula to calculate width increase of printed samples after 5 days of incubation in PBS 7.4

2.11 | Predictive Model for Printability

A predictive model was developed with RStudio [49] to evaluate the printability of hydrogels and to predict the printability of new formulations obtained with the same crosslinking chemistry and base materials but varying their relative concentrations. The model was

based on the calculation of a printability score, which is a custom-defined parameter used as an outcome measure to represent both the resolution of the 3D printing process and its fidelity to the original model. It was calculated by combining three experimentally derived parameters calculated before (PA, UF and SR), normalized to a 0–1 range, and combined according to Equation (10), where w_1, w_2, and w_3 represent weighting coefficients that determine the relative contribution of each term to the overall printability index. Several models were developed by varying these weighting coefficients to identify the most appropriate configuration and assess the influence of each parameter on printing resolution.

$$\text{Printability score} = \frac{w_1 \cdot PA + w_2 \cdot UF + w_3 \cdot SR}{w_1 + w_2 + w_3} \quad (10)$$

Equation 10. Formula to calculate the printability score, where w_1, w_2, and w_3 are the weighting coefficients that determine the relative contribution of each term to the overall printability index

In the baseline model, equal weights were assigned ($w_1 = w_2 = w_3$), resulting in a simple arithmetic mean of the normalized parameters. Initially, the parameters most suitable for the model were selected by comparing the material and mechanical properties of the hydrogels. Subsequently, to optimize the model, the input variables were expressed as the moles of functional groups involved in the crosslinking reaction rather than their masses. This conversion accounted for the DoF, previously determined by ^{1}H-NMR analysis. Different linear regression models were then developed to describe the relationship between the printability index and the composition of the hydrogels. To increase the number of input data points, hydrogel formulations that were initially excluded based on swelling tests were also included in the analysis. Model 1 was defined using the normalized printability index (equal weights, $w_1 = w_2 = w_3$) as the dependent variable and the molar concentrations of thiolated groups from Gel-SH and HA-SH together with PEG-NB as predictors. Model 2 introduced a z-score weighted printability index, in which the relative contribution of each experimental parameter was adjusted according to predefined weights. The weights were empirically assigned based on the estimated influence of each parameter on final printing resolution. PA reflects how closely the 3D-printed structure matches the original model and was therefore considered the most representative parameter of printability; accordingly, it was assigned a weight of 0.5. UF assesses the geometry of the printed pores relative to the 3D model and was given a slightly lower weight (0.4), as it was considered less critical than PA. Finally, SR evaluates the reliability of filament deposition and is less directly related to shape fidelity, making it the least important among the three parameters (−0.1). SR was assigned a negative weight because higher values correspond to poorer printing performance, unlike PA and UF, where higher values indicate better print quality. Model 3 applied custom weighting factors derived from regression coefficients obtained by fitting the printability index to the standardized (z-scored) parameters, providing a data-driven weighting scheme. In Model 4, the degree of crosslinking (DoC), defined as the molar ratio between total thiol groups and PEG-NB, was included as the main predictor, allowing the model to capture the effect of the network crosslinking density on printability. In this model, equal weights were used consistently with Model 1. Finally, Model 5 combined the data-driven weighted printability index from Model 3 with the DoC as predictor, resulting in a simplified model linking printability directly to the extent of crosslinking in the hydrogel formulation. All models were implemented in R using the lm() function, and predicted printability values were clipped between 0 and 1 to ensure a normalized output range. Developed models are described in Table 1.

To evaluate the predictive capability of the models, three new hydrogel formulations were considered, with varying amounts of Gel-SH, HA-SH, and PEG-NB. For each formulation, the moles of thiolated Gel/HA and PEG-NB were calculated, and the DoC was derived as the molar ratio between thiol groups and PEG-NB. Predicted printability indexes for each formulation were obtained using Models 1–5, applying the same formulas and weights as described previously. Experimentally, the new hydrogels were 3D printed, and the corresponding printing parameters were measured. Observed printability indexes were then calculated using the same formulas and weighting schemes as for the models, ensuring direct comparability between predicted and observed values. The performance of each model was evaluated by comparing predicted and observed printability indexes. Additionally, the predictive performance of the models was evaluated by calculating the Mean Absolute Error (MAE, Equation (11)) and the Root Mean Square Error (RMSE, Equation (12)) on three independent formulations used as validation set [50, 51]. These metrics, which quantify the average deviation between predicted and experimental values, were computed using the scikit-learn library in Python.

$$MAE = \frac{1}{n}\sum_{i=1}^{n} |y_i - \hat{y}_i| \quad (11)$$

Equation 11. Formula to calculate MAE, where y_i is the experimental value, $\hat{y}_i$ is the predicted value, and n is the number of samples.

$$RMSE = \sqrt{\frac{1}{n}\sum_{i=1}^{n} (y_i - \hat{y}_i)^2} \quad (12)$$

Equation 12. Formula to calculate RMSE, where y_i is the experimental value, $\hat{y}_i$ is the predicted values, and n is the number of samples.

The ML-assisted workflow to predict hydrogels printability is shown in Figure 1. The model development strategy focused on reducing the number of input variables by selecting high-impact mechanistic descriptors, such as the molar quantity of reactive groups and the degree of crosslinking (DoC), instead of relying on raw material masses. By using these chemically meaningful features, the model was better regularized against common challenges in small datasets, including overfitting and high variance, resulting in improved predictive stability. Data quality and chemical relevance were prioritized over data quantity, following modern ML approaches that use physical constraints to improve reliability.

2.12 | Statistical Analysis

Data were collected from samples produced in triplicate for each experiment. Quantitative results are reported as mean ± standard deviation (SD) (MS Excel). The number of significant figures for

TABLE 1 | Summary of ML models developed to predict printability index of hydrogels.

Model	Dependent variable	Predictors	Weighting scheme	Rationale
1	Normalized printability index	Molar concentrations of thiolated groups and PEG-NB	Equal weighting of printability components	Baseline model using unweighted, normalized printability index to evaluate direct relationship between formulation chemistry and printability
2	z-score printability index	Molar concentrations of thiolated groups	Empirical fixed weights: PA = 0.5, UF = 0.4, SR = −0.1	Combined empirically weighting reflecting relative importance of printability metrics
3	z-score printability index	Molar concentrations of thiolated groups	Data-driven weights derived from regression coefficients of standardized parameters	Fully data-driven model where weights reflect statistical contribution of each parameter to printability
4	Printability index	DoC	Equal weighting of printability components	Evaluates predictive power of network crosslinking density as a single mechanistic descriptor of printability
5	Printability index	DoC	Data-driven weights derived from regression coefficients of standardized parameters	Simplified mechanistic-data hybrid model linking printability directly to hydrogel crosslinking extent

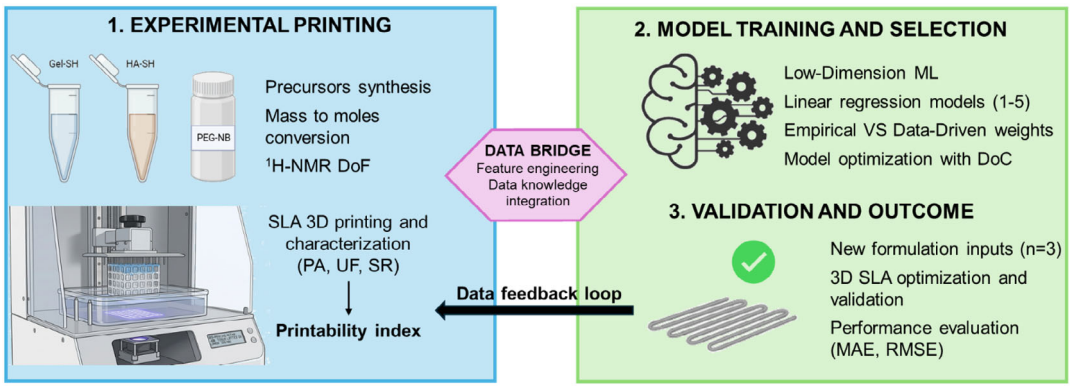

FIGURE 1 | ML-assisted workflow to predict hydrogels printability.

quantitative characterizations was determined based on the precision of the measuring instruments. Specifically, biological assay results were rounded to two decimal places, while ML performance metrics (MAE and RMSE) and regression coefficients were maintained at four decimal places to ensure model sensitivity and comparability. Statistical analysis was performed using one-way ANOVA in OriginPro 2022b, followed by Tukey's post hoc test for multiple comparisons. A p-value <0.05 was considered statistically significant. Tukey's method identifies specific group pairs with significant differences by comparing all possible mean combinations using the studentized range distribution [52, 53].

3 | Results

3.1 | Functionalization of Gelatin with Thiol Groups (Gel-SH)

Gel-SH was obtained by promoting the nucleophilic attack of lysine-exposed amino groups on the carboxylic group of γ-thiobutyrolactone (Figure 2) [54]. The reaction, performed at 37°C, was adapted from a previous work [55]. Briefly, Gel (1 g, 10% w/V) was dissolved in 0.1 M buffer bicarbonate pH 10 in a round flask. Once fully dissolved, 0.45 mL γ-thiobutyrolactone was added at three different time points, waiting 30 min before each addition. It was added in excess to increase the functionalization. The solution was left under stirring overnight. Subsequently, 264 mg DTT was added to the solution which was left under stirring for another 24 h. The product (Gel-SH) was dialyzed 24 h with 0.1 M NaCl and 48 h against deionized water, changing the dialysis solution four times per day, filtered (0.22 µm filter), freeze-dried using Vacuum Freeze Dryer (Boyikang Laboratory Instruments Inc, Beijing, China) for 48 h at $T = -50$°C and pressure below 15 Pa and stored at −20°C until further use.

The functionalization effectiveness was qualitatively evaluated with ^{1}H-NMR analysis, comparing Gel-SH and Gel spectra (Figure 4A). The peak corresponding to -CH_2NH_2 lysine at 2.9 ppm (pink dot) significantly diminishes, indicating their involvement in the reaction as conversion into a -CH_2NH- group.

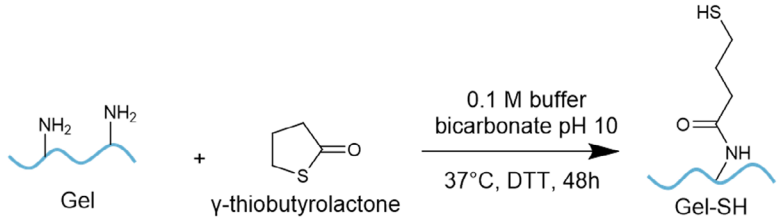

Gel	1
γ-thiobutyrolactone	15
DTT	5

FIGURE 2 | Functionalization of gelatin with thiol groups, the equivalents are calculated based on the assumption that in mean gelatin has 5% lysines.

Furthermore, new peaks at 2.55 and 1.53 ppm appear in Gel-SH spectrum, which are characteristic of protons adjacent to a thiol group, confirming the effectiveness of the reaction. The DoF was calculated through Ellman's assay: DTNB, upon reaction with free thiols of proteins, generates a colored product (2-nitro-5-thiobenzoate, TNB) that absorbs at 412 nm [56]. The DoF was estimated by comparing the absorbance of Gel-SH to a calibration curve (Supporting Information S.1.), and the value obtained was 7.03%, indicating a full functionalization of lysine groups.

3.2 | Functionalization of Hyaluronic Acid with Thiol Groups (HA-SH)

HA-SH was obtained by condensation of the carboxylic acid of HA with cysteamine exploiting EDC and NHS as condensing agents (Figure 3). Briefly, hyaluronic acid (HA, 500 mg, 0.5% w/V) was dissolved at 50°C in dH2O, adjusting pH to 5.5 using 0.1 M NaOH solution. After dissolution, 2.33 g EDC and 0.46 g NHS were added to the reaction mixture, meanwhile cysteamine (500 mg, 5% w/V) was dissolved in dH2O. After 30 min, cysteamine solution was added dropwise to the reaction mixture, which was left under stirring at room T overnight. Subsequently, 1 g DTT was added and left for 1 h under temperature-controlled sonication. The product (HA-SH) was dialyzed 24 h with 0.1 M NaCl and 48 h against deionized water, changing the dialysis solution four times per day, filtered (5 μm filter), freeze-dried using Vacuum Freeze Dryer (Boyikang Laboratory Instruments Inc, Beijing, China) for 48 h at $T = -50$°C and pressure below 15 Pa and stored at −20°C until further use.

In Figure 4B, its spectrum is shown compared to HA spectrum. The characteristic peaks of cysteamine at 2.44, 2.69 and 2.91 ppm are also present in HA-SH spectrum, confirming the functionalization. The total amount of cysteamine linked to HA was determined by comparing the area of the peak at 2.91 ppm, which corresponds to protons adjacent to the amino group, to the TMSP reference peak at 0 ppm, resulting in 20.70% substitution. The peak at 2.44 ppm indicates the presence of protons adjacent to an oxidized thiol group. The actual quantity of free-thiol groups was therefore calculated using the peak at 2.69 ppm, which corresponds to protons next to a free thiol group, yielding a value of 5.33%. This result was confirmed by Ellman's assay, which gave a similar value of 5.48%. To increase the quantity of free-thiol groups, HA-SH can be treated with DTT under sonication. After adding 0.15% w/w of DTT, the Ellman's assay gave a result of 15.30%.

3.3 | Thiol–Ene Photoclick Hydrogel Formation

Hydrogels were prepared using radical thiol–norbornene step-growth photopolymerization [27]. This process is initiated by UV light, which generates thiyl radicals that react with alkenes by directly breaking bonds in thiols, and photoinitiators are used to enhance the efficiency of the reaction [58]. The scheme of the reaction is shown in Figure 5. Briefly, Gel-SH, HA-SH, and PEG-NB solutions were mixed, and the crosslinking mechanism was initiated by a light-sensitive initiator, specifically LAP. DTT was added prior to LAP to prevent the oxidation of thiol groups to maximize crosslinking.

In all formulations, gelation occurred immediately upon UV light exposure of the precursor solution; however, to ensure better crosslinking stability, the hydrogels were exposed to UV light for 180 s. Figure 6 shows the appearance aspect of the hydrogels immediately after formation, with no significant differences observed in the external appearance between six formulations.

Six different formulations were designed by varying the concentrations of Gel-SH, HA-SH, and PEG-NB (Table 2). The concentration 70 mg/mL of PEG-NB was determined to ensure equal amounts of photo-crosslinkable moieties, considering DoF of materials. Subsequently, the amount of PEG-NB was decreased

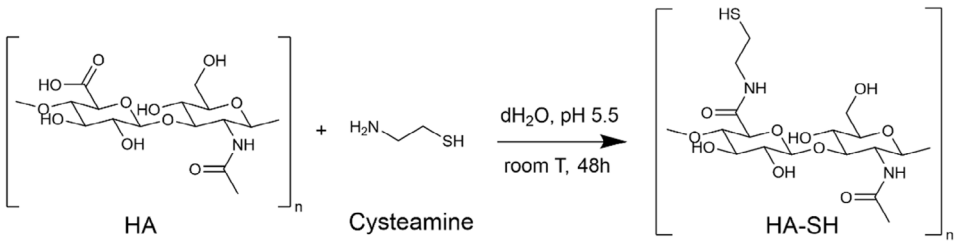

HA	1
Cysteamine	5
EDC	9
NHS	3
DTT	5

FIGURE 3 | Functionalization of HA with thiol groups.

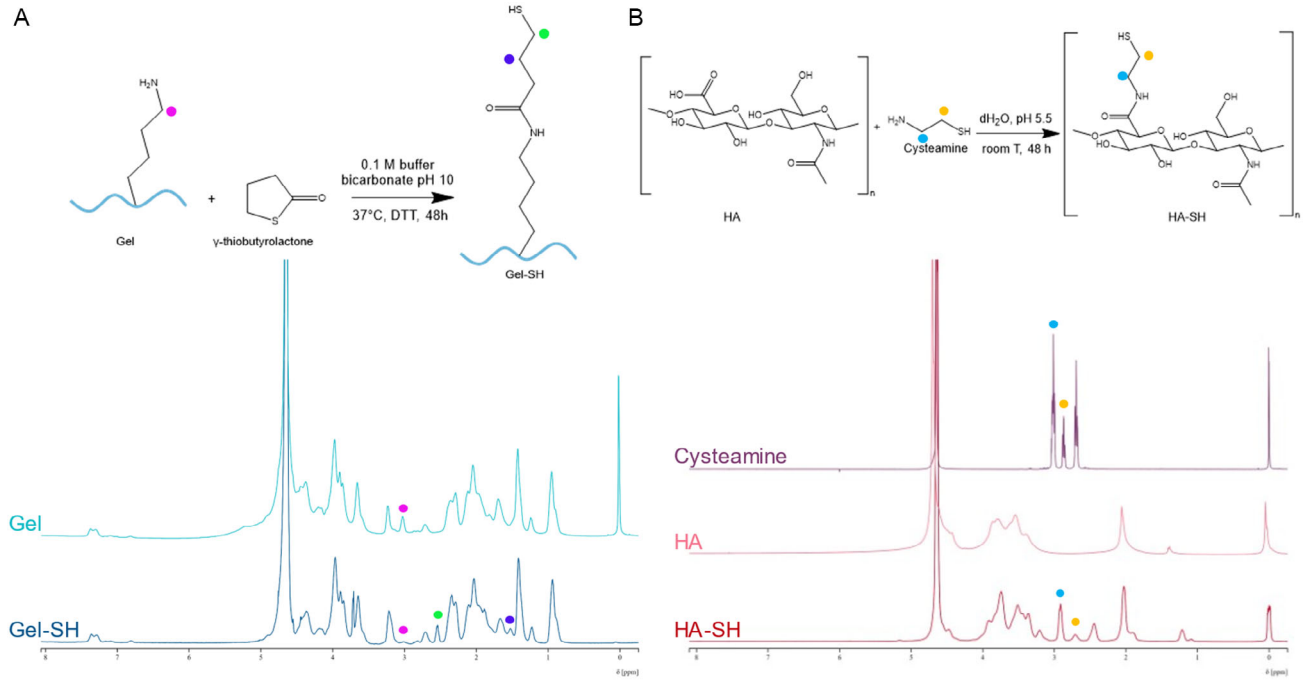

FIGURE 4 | ^{1}H-NMR spectra of Gel, Gel-SH, HA, HA-SH, and cysteamine. In Gel-SH, functionalization was confirmed by a decrease in the characteristic peaks of ε-methylene protons (epsilon protons) of the lysine side chain at 2.9 ppm (pink dot) and by the appearance of characteristic peaks of protons adjacent to a thiol group at 2.55 and 1.53 ppm. In HA and HA-SH, the characteristic peaks of the protons in the sugar rings are found between 3 and 3.8 ppm [57]; otherwise in HA-SH, characteristic peaks of cysteamine are observed at 2.44, 2.69 ppm (orange dot), and 2.91 ppm (light-blue dot), confirming the effectiveness of the reaction.

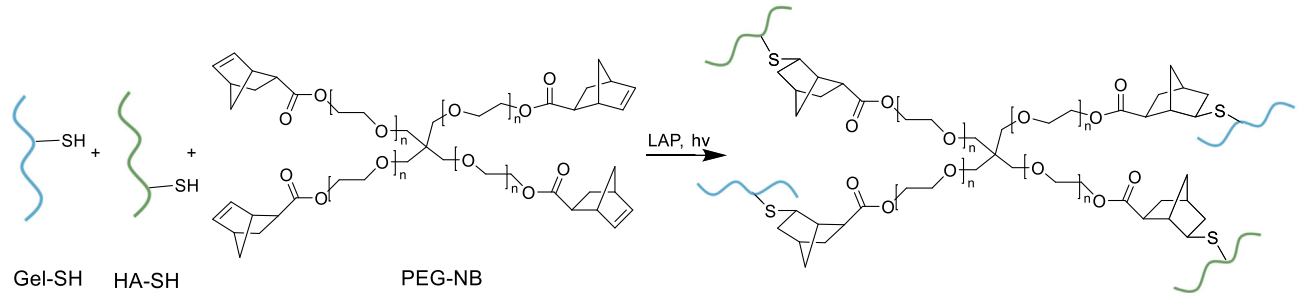

FIGURE 5 | Scheme of the thiol–ene photoclick hydrogel formation.

to adjust the norbornene–thiol ratio, allowing for excess functional moieties to facilitate the selective attachment of target molecules. In all cases, the procedure was as follows: First, PEG-NB, Gel-SH, and HA-SH each were dissolved in DPBS 7.4 at 37°C. Then, the three solutions were mixed to form the hydrogel's precursor solution. After the addition of 0.1% w/V DTT, a reducing agent that breaks disulfide bonds, and 10 mM LAP as photoinitiator, photochemical crosslinking reaction was induced by exposure to 405 nm wavelength UV light.

The effectiveness of hydrogels formation was qualitatively and quantitatively verified through ^{1}H-NMR analysis, comparing their spectra with their respective Gel-SH, HA-SH, and PEG-NB not crosslinked blend. In this case, hydrogels were formed and crosslinked directly in NMR glass tubes. The percentage reduction of the characteristic PEG-NB double peaks at 5.99 and 6.25 ppm was calculated using Equation (13).

$$\text{peaks reduction}\,[\%] = \frac{\int PEG-NB\,\text{peaks}\,no\,link}{\int PEG-NB\,\text{peaks}\,link} \cdot 100 \qquad (13)$$

Equation 13. Formula to calculate the percentage reduction of PEG-NB characteristic peaks after crosslinking, where "no link" indicates before crosslinking and "link" after crosslinking.

3.4 | Swelling Test

A swelling test was carried out as a preliminary characterization on the six formulations. The test was performed at three different pH values (5.5, 7.4, and 8.5) as human tissues are characterized by various pH, and the results obtained are displayed in Figure 7. A decrease in swelling indicates that the hydrogel microstructure is beginning to break down due to the high amount of absorbed liquid, leading to degradation.

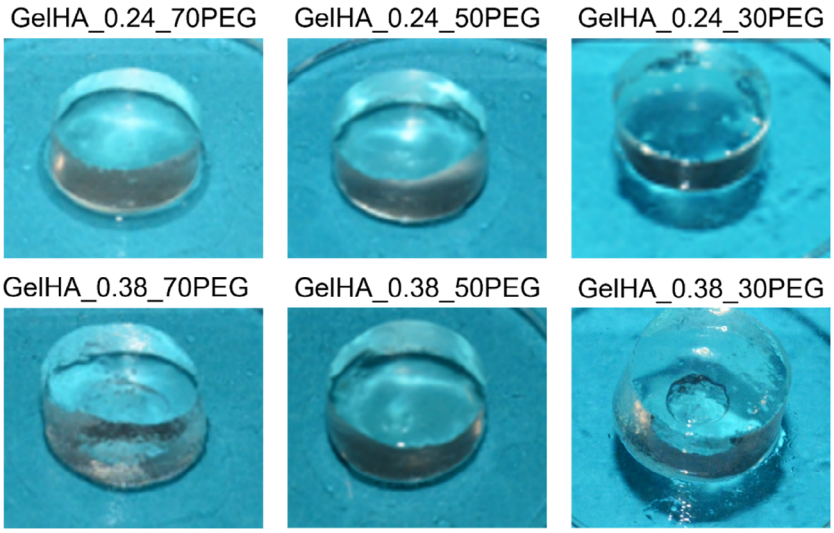

FIGURE 6 | Hydrogels appearance after UV light-induced gelation.

TABLE 2 | Thiol–ene photoclick hydrogel formulations obtained varying Gel-SH, HA-SH, and PEG-NB concentrations. EQ are equivalents.

Name	EQ -SH groups Gel-SH	EQ -SH groups HA-SH	c Gel-SH (mg/mL hydrogel)	c HA-SH (mg/mL hydrogel)	c PEG-NB (mg/mL hydrogel)
GelHA_0.24_70PEG	1	0.24	18	2	70
GelHA_0.24_50PEG	1	0.24	18	2	50
GelHA_0.24_30PEG	1	0.24	18	2	30
GelHA_0.38_70PEG	1	0.38	17	3	70
GelHA_0.38_50PEG	1	0.38	17	3	50
GelHA_0.38_30PEG	1	0.38	17	3	30

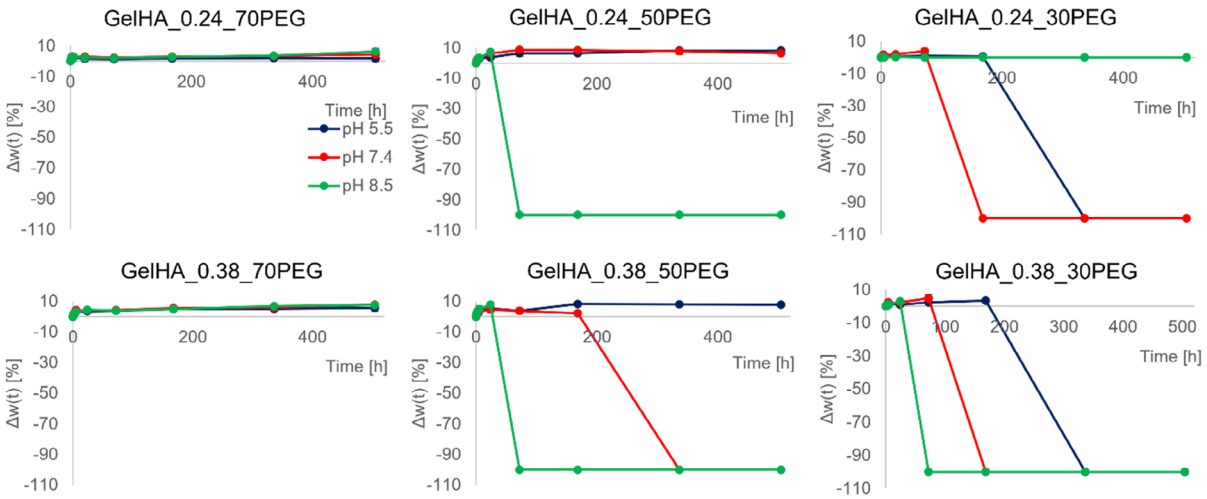

FIGURE 7 | Swelling test results at pH 5.5 (blue lines), 7.4 (red lines), and 8.5 (green lines).

Formulations GelHA_0.24_70PEG and GelHA_0.38_70PEG, characterized by higher PEG-NB concentrations, exhibited greater resistance to pH-induced changes over time. In both cases, the swelling rate increased with rising pH. Notably, GelHA_0.38_70PEG absorbed more PBS, likely due to its higher HA-NB content, which has known water-retention properties. In contrast, the hydrogels GelHA_0.24_50PEG and GelHA_0.38_50PEG performed poorly at pH 8.5: although initial swelling was observed, they fully degraded before day 5. Additionally, the formulation with higher HA-SH content degraded by day 7 even at neutral pH. Interestingly, the two 50PEG formulations showed distinct swelling behaviors: GelHA_0.24_50PEG swelled similarly at pH 5.5 and 7.4, while GelHA_0.38_50PEG showed significantly greater swelling at

pH 5.5. Unfortunately, formulations GelHA_0.24_30PEG and GelHA_0.38_30PEG exhibited a poor performance, totally degrading at every pH by day 7. Formulations GelHA_0.24_30PEG and GelHA_0.38_30PEG showed poor performance, fully degrading at all tested pH levels by day 7. Due to their instability under neutral conditions, GelHA_0.38_50PEG, GelHA_0.24_30PEG, and GelHA_0.38_30PEG were excluded from further analysis. In contrast, GelHA_0.24_70PEG and GelHA_0.38_70PEG demonstrated greater stability and consistent behavior across different pH levels and were selected for further characterization. GelHA_0.24_50PEG was also included due to its favorable swelling properties at pH 7.4.

3.5 | Real-Time ^{1}H-NMR

Hydrogel formation was qualitatively verified with ^{1}H NMR analysis, comparing their spectra with their respective Gel-SH, HA-SH, and PEG-NB not crosslinked blend (Figure 8). In GelHA_0.24_50PEG and GelHA_0.38_70PEG formulations, the characteristic peaks of the norbornene double bond at 5.99 and 6.25 ppm were largely absent following gelation, indicating a high DoC. In contrast, for GelHA_0.24_70PEG, these peaks were reduced but still detectable, suggesting that a portion of the norbornene groups remained unreacted. Quantitative analysis confirmed these observations, with peak reductions of 68.3%, 86.9%, and 89.9% for GelHA_0.24_70PEG, GelHA_0.24_50PEG, and GelHA_0.38_70PEG, respectively.

3.6 | Amplitude Sweep and Compression Tests

Rheological characterization of the hydrogels was performed using amplitude sweep measurements to identify the linear viscoelastic region (LVR), defined as the range where the complex stress increases linearly with oscillatory strain, and both G′ and G″ remain constant. Figure 9 presents the results for the three formulations tested. All hydrogels exhibited a similar LVR, extending up to approximately 1% strain, beyond which G″ began to show strain-dependent behavior, while G′ remained stable up to 8%–10% strain. Notable differences were observed in the absolute values of G′ and G″: GelHA_0.24_50PEG showed the lowest G′ (960 Pa) and G″ (7 Pa), while GelHA_0.24_70PEG displayed the highest values (G′ = 2565 Pa; G″ = 27 Pa). Yield strain ranged between 8.0% and 10.5%, whereas the flow point varied more substantially. GelHA_0.24_50PEG demonstrated the highest flow strain, breaking at 267.5% deformation. These results suggest that PEG-NB concentration plays a key role in determining hydrogel viscoelasticity: higher PEG-NB content enhances both G′ and G″, while reducing the deformability of materials.

Compression test was performed on cylindrical hydrogel specimens to assess their mechanical properties (Figure 10). The initial elastic region of the stress–strain curve was analyzed to determine key parameters, including E, σ_y, and ε_y. GelHA_0.38_70PEG exhibited the highest stiffness (170.9 kPa), while GelHA_0.24_70PEG and GelHA_0.24_50PEG showed comparable, lower values (15.3 and 15.9 kPa, respectively). In terms of ε_y, GelHA_0.24_50PEG reached plastic deformation at 11.1%, whereas the other two hydrogels remained in the elastic region at 15.0% strain, with yield points of 16.1% (GelHA_0.24_70PEG) and 17.2% (GelHA_0.38_70PEG), suggesting greater elasticity. At 25% strain, GelHA_0.38_70PEG also demonstrated the highest stress (58.3 kPa), followed by GelHA_0.24_50PEG (17.2 kPa) and GelHA_0.24_70PEG (11.2 kPa). These results indicate that HA content, rather than PEG concentration, plays a more significant role in determining the mechanical strength of the

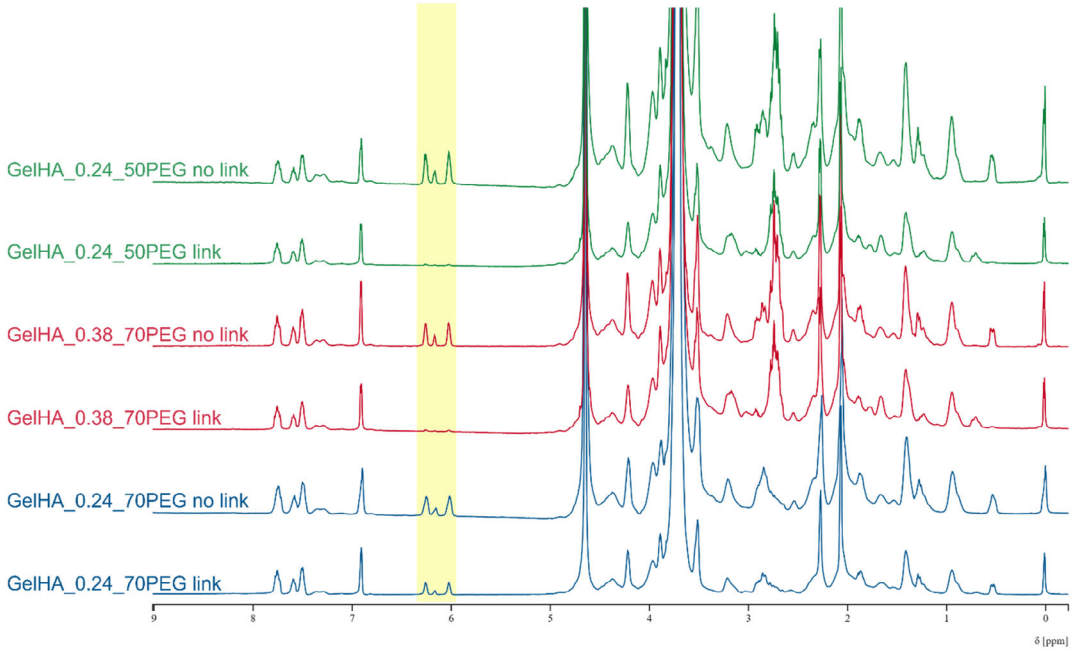

FIGURE 8 | ^{1}H NMR spectra of the four hydrogels before and after gelation, where "no link" indicates formulations before crosslinking and "link" after crosslinking. As a proof of the involvement of the norbornene units during the gelation process, the peaks of vinylic protons either disappeared or diminished.

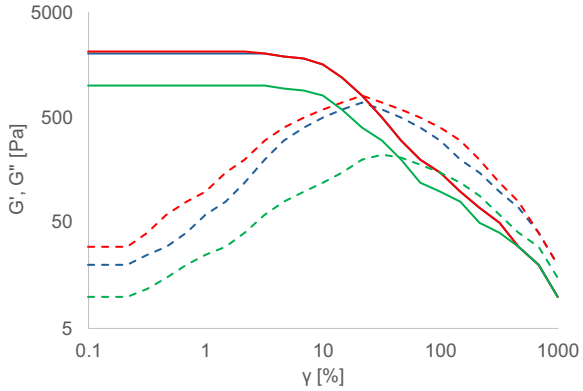

Formulation	G' [Pa]	G" [Pa]	γ_Y [%]	γ_F [%]
GelHA_0.24_70PEG	2565	27	8.5	90.2
GelHA_0.38_70PEG	2270	17	8.4	127.5
GelHA_0.24_50PEG	960	7	10.5	267.5

FIGURE 9 | Amplitude sweep test showing G' (continuous line) and G" (dashed line) as functions of γ. Yield strain (γ_y) and flow strain (γ_F) points were also identified for each formulation.

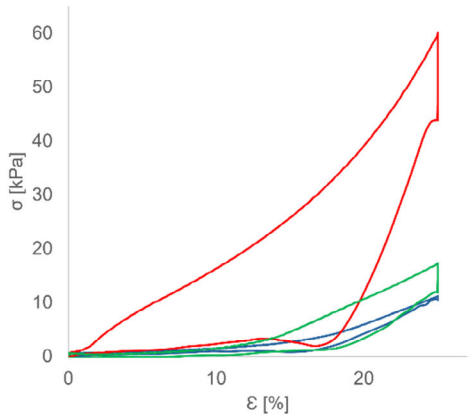

Formulation	E [kPa]	ε_y [%]	σ_y [kPa]	σ_{25} [kPa]	% hystheresis at ε = 25%
GelHA_0.24_70PEG	15.3	16.1	3.2	11.2	69.1
GelHA_0.38_70PEG	170.9	17.2	28.2	58.3	32.5
GelHA_0.24_50PEG	15.9	11.1	1.9	17.2	38.4

FIGURE 10 | Stress–strain curves obtained from compression tests with 25% deformation, a 10-s hold, and unload test.

hydrogels. All samples exhibited pronounced hysteresis between loading and unloading curves, indicating plastic deformation without structural failure. This effect was most evident in GelHA_0.24_70PEG, which showed 69.1% permanent deformation, compared to 32.5% and 38.4% in GelHA_0.24_50PEG and GelHA_0.38_70PEG, respectively.

3.7 | SEM Analysis

The results of the SEM analysis are presented in Figure 11. Images were acquired in high-resolution mode at a magnification of 500X. Prior to imaging, all samples were frozen at −20°C overnight and then stored at −80°C until lyophilization. All hydrogels

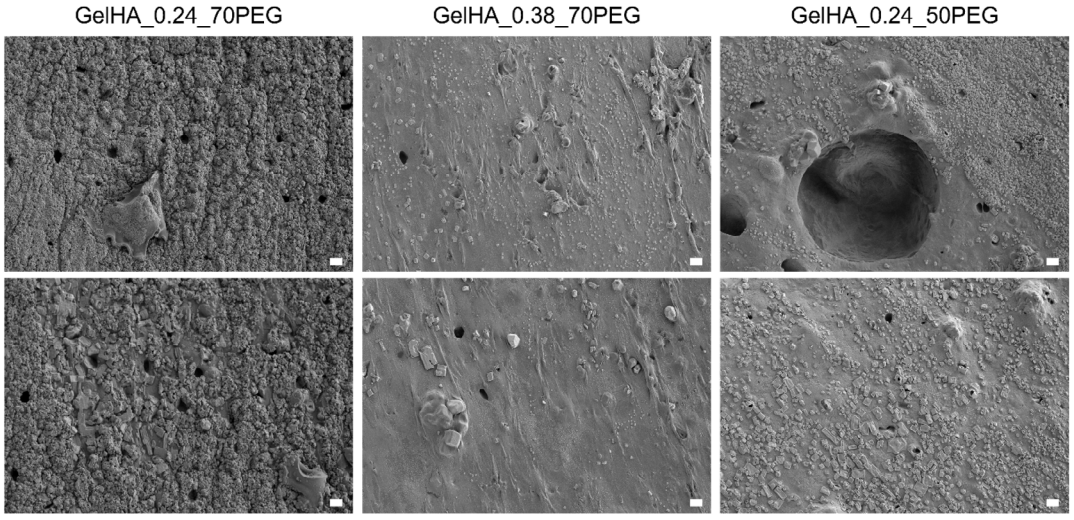

FIGURE 11 | SEM images of hydrogel cross-sections, magnification: 500X, scale bar: 20 μm.

exhibited relatively homogeneous surfaces, a feature likely attributed to the crosslinking strategy. The small size of the functional groups used for Gel and HA modification (γ-thiobutyrolactone and cysteamine, respectively) promotes the formation of a compact polymer network via the thiol–ene reaction. Formulations GelHA_0.24_70PEG and GelHA_0.38_70PEG displayed pores with diameters around 5 μm, whereas GelHA_0.24_50PEG showed considerably larger pores ranging from 20 to 100 μm. This difference in pore size is likely due to the lower PEG-NB content, which provides fewer norbornene groups for crosslinking and results in a more open, less dense network structure.

3.8 | Indirect Cytotoxicity and Direct Cytocompatibility Tests

An indirect cytotoxicity test was conducted on the GelHA_0.24_70PEG formulation, selected as the worst-case scenario due to its higher PEG-NB content, a component that could potentially cause adverse cellular responses. Furthermore, ^{1}H-NMR analysis revealed the presence of unreacted PEG-NB in this formulation, reinforcing its designation as the most critical condition. Consequently, if this formulation is confirmed to be non-cytotoxic, it can be reasonably inferred that the other formulations, with either lower PEG-NB concentrations or more complete crosslinking, are also non-cytotoxic. The results of the cytotoxicity test on the GelHA_0.24_70PEG formulation are shown in Figure 12A, with cells cultured directly on well plates used as the control group (CTRL). Tukey's test enabled the identification of samples with comparable biological behavior, as indicated by shared letters in the table presented in Supporting Information S.2. No statistically significant differences were found between GelHA_0.24_70PEG and the control group at any time point, confirming that PEG-NB crosslinking did not induce cytotoxicity. Additionally, based on ISO 10993-5, which defines a 70% viability threshold, the formulation is classified as non-cytotoxic [37].

A direct cytocompatibility test was performed on all formulations to evaluate their ability to support cell adhesion and proliferation. Due to the low porosity observed by SEM and the notable mechanical characteristics of the hydrogels, two seeding conditions were tested: hBM-MSCs seeded on the hydrogel surface after crosslinking, and cells mixed into the formulations before crosslinking. Cell metabolic activity was assessed at multiple time points using the Alamar Blue assay and absorbance values were recorded and normalized to day 1 to monitor cell growth over time. The results are shown in Figure 12B,C.

During the initial days of culture, all formulations exhibited comparable levels of metabolic activity. However, from day 10 onward, cells seeded on the hydrogel surface demonstrated higher metabolic activity compared to those embedded within the matrix, with the difference becoming more pronounced by day 21. While CTRL consistently showed the highest metabolic activity across all time points, the gap between the control and the surface-seeded samples was notably reduced by day 21. To further evaluate statistical differences among the groups, a

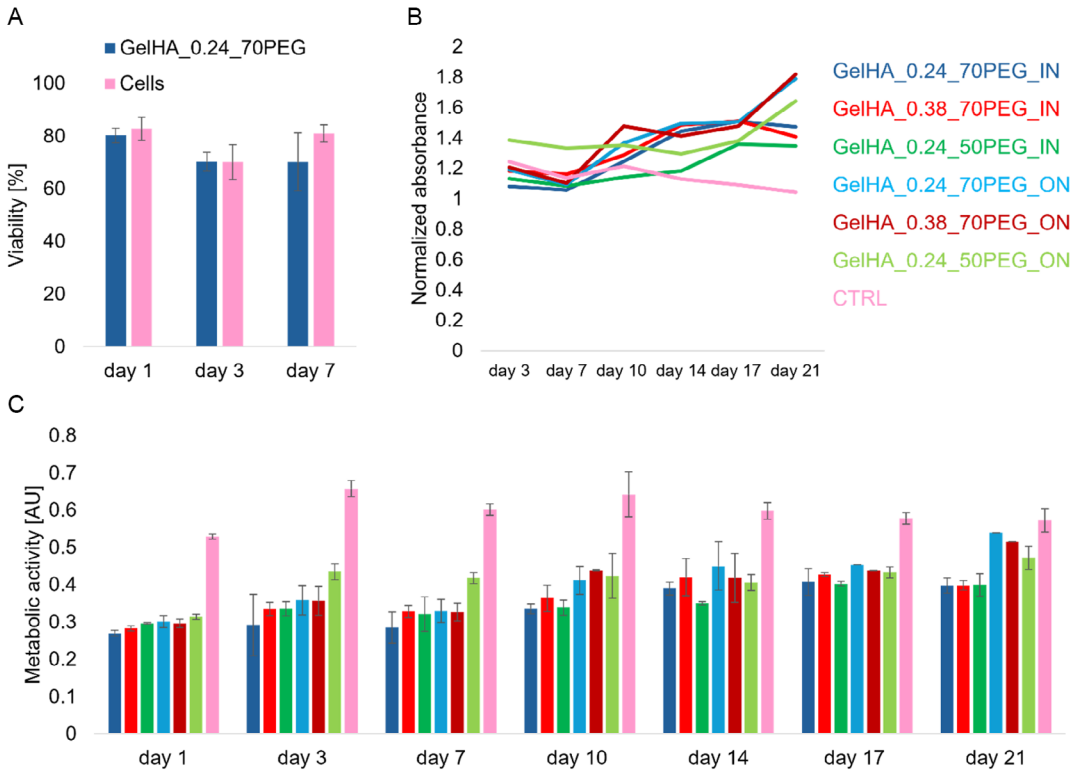

FIGURE 12 | Viability of hBM-MSCs assessed at days 1, 3, and 7 during the cytotoxicity test (A). Metabolic activity measured by absorbance (B), and absorbance values normalized to day 1 obtained during the cytocompatibility test up to day 21 (C). Cells seeded on well plates were used as controls (CTRL).

one-way ANOVA followed by Tukey's post hoc multiple comparisons was performed, and the resulting table is reported in Supporting Information S.3. Although many groups are present, CTRL samples are mostly grouped together, but also include hydrogels with cells seeded on the surface at days 17 and 21. Another big group can be individuated between hydrogels with cells on the surface at intermediate time points and hydrogels with cells inside at time points 14, 17, and 21, and finally hydrogels with cells inside at time points 1, 3, and 7, with lowest absorbance values. Regarding the overall comparison among hydrogels, excluding controls, no major differences are present with hydrogels with cells inside, although regarding cells on the surface GelHA_0.24_70PEG has the highest metabolic activity and GelHA_0.24_70PEG the lowest.

3.9 | Morphological Characterization of Cells

Live-Dead analysis was carried out to investigate differences in cell morphology among hydrogel formulations and seeding conditions. Brightfield images were acquired prior to fluorescence microscopy, and representative results are provided in Supporting Information S.3. Images were taken at two distinct regions of each hydrogel to evaluate cell distribution and potential migration from the surface. In hydrogels containing cells within the matrix, cells remained rounded throughout the 21-day culture, with only a slight increase in density in GelHA_0.24_70PEG_IN and GelHA_0.24_50PEG_IN. This limited spreading is likely related to the high stiffness and low porosity of the matrices, combined with the higher Gel content that promotes adhesion via RGD sequences. In contrast, cells seeded on the hydrogel surface initially formed aggregates visible from day 1 to day 7, progressively elongating and adhering to the surface. Starting from day 7, cell migration into the hydrogel bulk was observed, with the number of migrating cells increasing progressively over time. Among the different formulations, GelHA_0.38_70PEG_ON showed limited migration from the surface, probably for the higher structural rigidity, whereas cells on GelHA_0.24_50PEG_ON exhibited more pronounced elongation compared to other groups.

To better investigate cell morphology, Live-Dead assays were performed at day 7 and day 14, with the results shown in Supporting Information S.4., and at day 21, with the results presented in Figure 13A. These observations confirmed what had been previously noted: cells embedded within the hydrogels remained rounded and evenly distributed throughout the bulk, whereas cells seeded on the surface initially formed aggregates and subsequently began migrating inward over time. Viability was also quantified, and the corresponding bar plot is shown in Figure 13B. In all formulations, viability remained above 95%, confirming the cytocompatibility of the hydrogels. ANOVA analysis revealed no statistically significant differences between groups (Supporting Information S.3.). In addition, Figure 13A reports fluorescent images of cells stained with Phalloidin and DAPI, highlighting actin filaments and nuclei, respectively. Qualitatively, encapsulated cells appeared at lower density and retained a rounded morphology, while surface-seeded cells were more elongated, particularly in formulations containing higher Gel content. To complement this observation, nuclei roundness was quantified using Fiji ImageJ, with the results presented as a violin plot in Figure 13C. As expected, GelHA_0.24_70PEG_ON and GelHA_0.24_50PEG_ON displayed lower roundness values (0.51 and 0.43, respectively), reflecting greater elongation and improved adhesion associated with higher Gel levels. Conversely, embedded cells in GelHA_0.24_70PEG_IN and GelHA_0.24_50PEG_IN showed higher roundness values (0.66 and 0.65), confirming that the mechanical stiffness of the network limited their ability to elongate. This finding was reinforced by GelHA_0.38_70PEG_ON and GelHA_0.38_70PEG_IN, which presented even higher roundness values (0.71 and 0.75, respectively), further supporting the conclusion that hydrogel stiffness is the major factor influencing cell elongation, with surface seeding partially mitigating this effect. Additionally, formulations with lower PEG content exhibited not only reduced mean roundness values but also greater variability, suggesting a broader heterogeneity in cell responses within these networks.

3.10 | 3D Printing Test

3D printing of hydrogels was performed to assess the suitability of the different formulations for additive manufacturing. Since crosslinking was induced by UV light, a Lumen X LDP 3D printer was selected for its ability to fabricate high-resolution structures. An STL file was designed with a mesh diameter of 0.4 mm, as shown in Figure 14.

The resulting prints are shown in Figure 15A. All formulations qualitatively demonstrated good printability, as the printed meshes closely resembled the STL design. To evaluate the goodness of printed constructs in biological-like conditions, samples were put for five days in PBS 7.4 with 0.02% w/V sodium-azide (Figure 15B). After incubation time, all samples swelled but maintaining their printed 3D structure, confirming their suitability to be used for tissue engineering purposes. To quantitatively evaluate print fidelity, parameters were measured under a microscope, accounting for the varying rheological and mechanical properties of the formulations. For SR, GelHA_0.38_70PEG and GelHA_0.24_50PEG both yielded values of 1.06, while GelHA_0.24_70PEG showed a slightly higher value, indicating a less accurate match between the theoretical and actual filament diameters. Nonetheless, as all SR values were close to 1, the overall shape fidelity can be considered high (Figure 15C). PA was assessed to evaluate the correlation between the printed constructs and the original 3D model. Formulations with higher Gel content exhibited higher PA values, with GelHA_0.24_50PEG reaching 96.4%. In contrast, GelHA_0.38_70PEG showed the lowest PA, with a value of 76.1% (Figure 15D). It should be noted, however, that the STL mesh diameter was very small, and therefore all obtained values can still be considered acceptable. Regarding UF, all values were below 1, reflecting slightly more rounded geometries in the printed models compared to the STL design (Figure 15E). The variation of width lengths after 5 days of incubation in PBS was also evaluated, with the resulting graph shown in Figure 15F. Values obtained for GelHA_0.24_70PEG and GelHA_0.38_70PEG are comparable, indicating that their swelling behavior is similar, confirming the swelling test performed in the previous chapter. Furthermore, GelHA_0.24_50PEG exhibited a slightly lower value, indicating that a lower PEG-NB quantity determines a lower water retention. All the calculated parameters are summarized in Figure 15G.

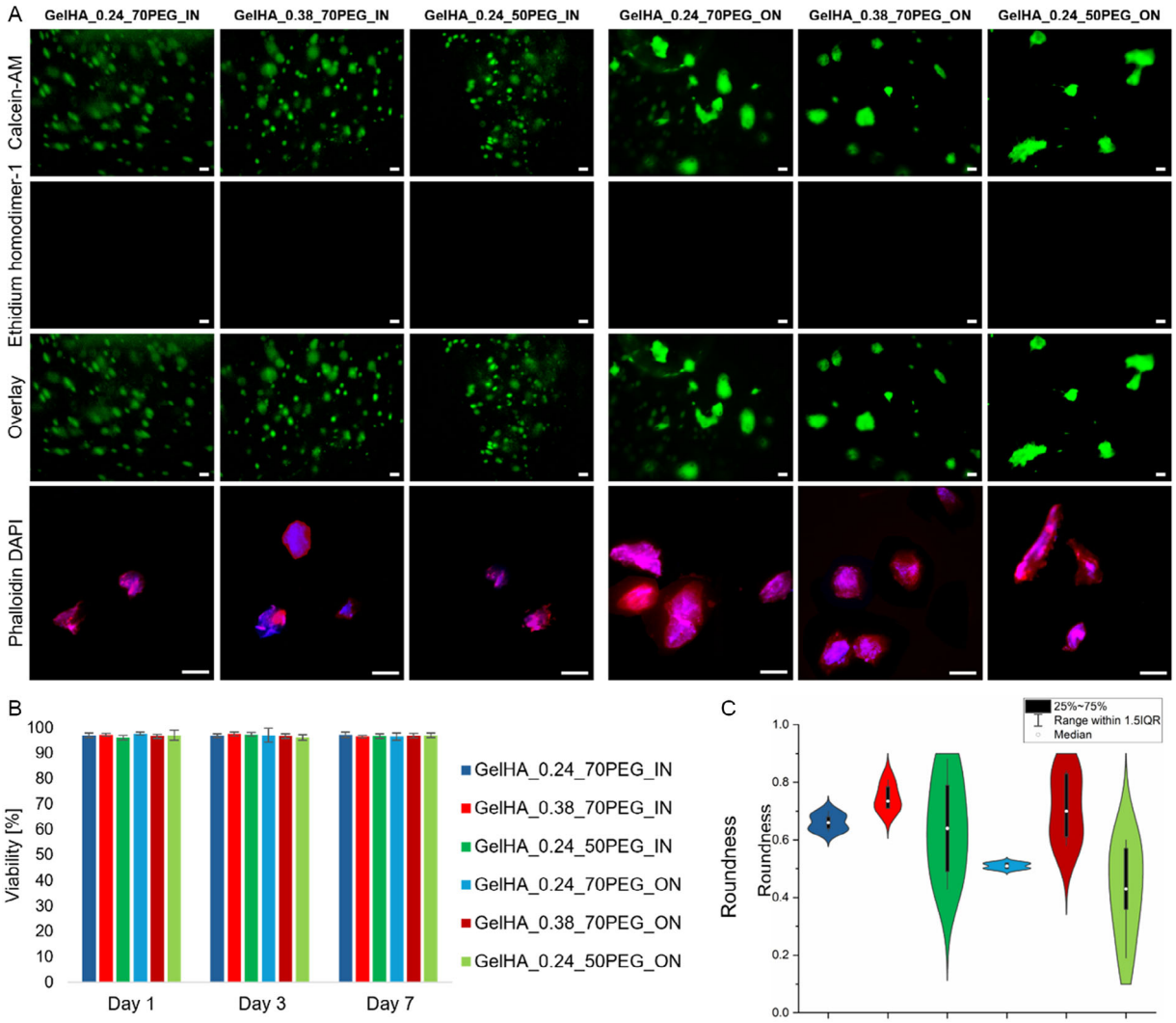

FIGURE 13 | Live-Dead (scale bar: 100 μm) and Phalloidin DAPI (scale bar: 20 μm) images taken on formulations after 21 days of culture (A), viability calculated with Live-Dead assay with standard deviation (SD) error bars (B) and cell roundness violin plot (C).

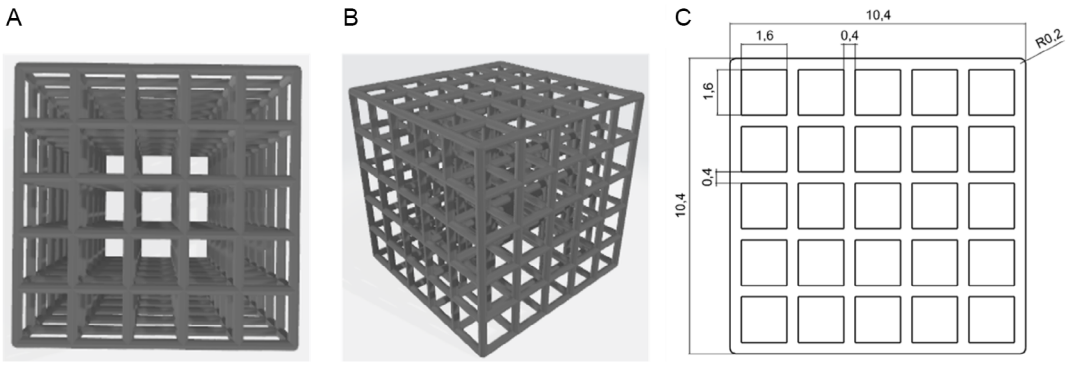

FIGURE 14 | Top (A) and isometric (B) views of STL model used for hydrogel 3D printing; 2D drafting of the designed 3D model, including the corresponding dimensions indicated in mm (C).

3.11 | Preliminary Predictive Model for Printability

A preliminary predictive model for the printability of hydrogels was developed based on printing parameters previously calculated. Cell viability was not included as a variable in the model because Gel and HA contents, as well as cell adhesion, were comparable in all formulations and the only observed differences concerned whether cells were seeded on the surface or within the hydrogels. In this model, printing parameters such as exposure time, first layer time scale factor, and projector power level were kept constant, as was the total material content of the

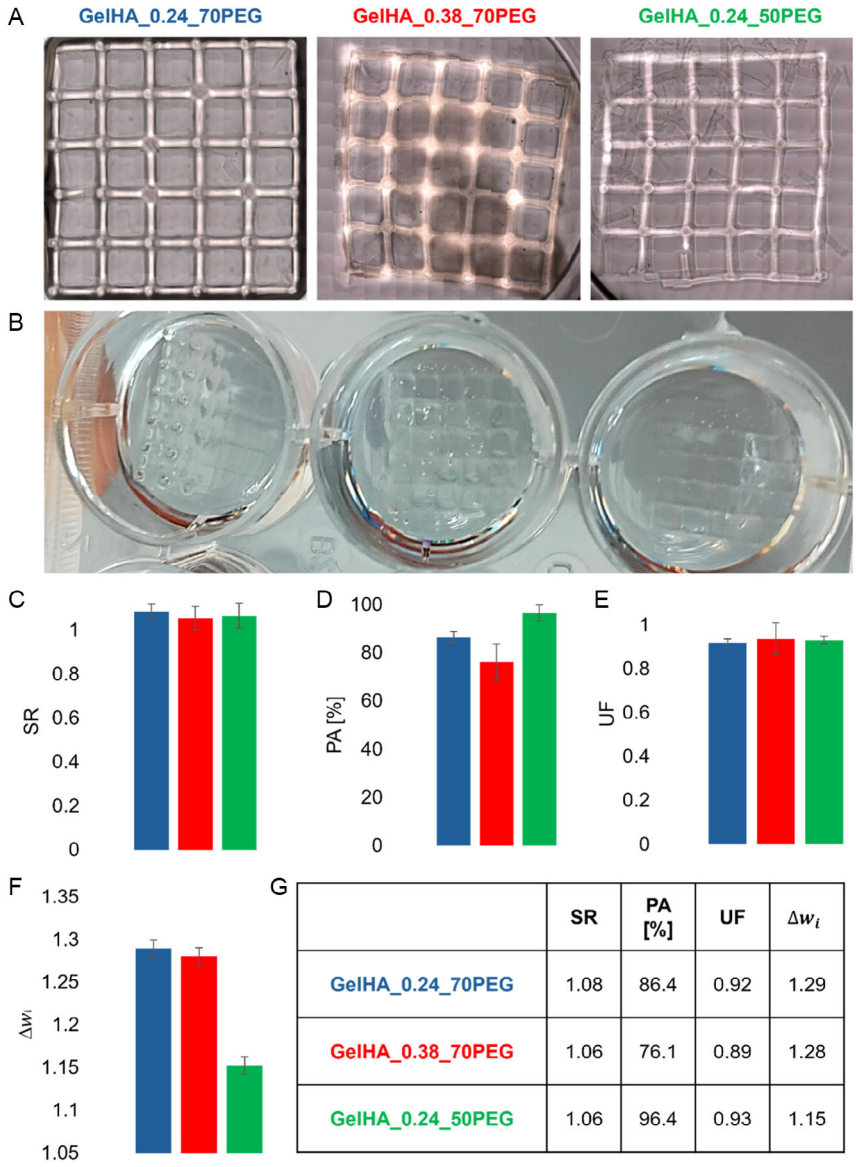

G

	SR	PA [%]	UF	Δw_i
GelHA_0.24_70PEG	1.08	86.4	0.92	1.29
GelHA_0.38_70PEG	1.06	76.1	0.89	1.28
GelHA_0.24_50PEG	1.06	96.4	0.93	1.15

FIGURE 15 | Hydrogels immediately after 3D printing (A) and after 5 days in PBS 7.4 (B); some printing parameters were calculated after microscope observation, such as swelling ratio (C), printing accuracy (D), uniformity factor (E) and variation of width length after 5 days in PBS 7.4 (F); data are expressed as mean ± SD in graphs, although in the table only the mean values are summarized (G).

hydrogels (2%), while other parameters were varied as input variables. To determine the most relevant predictors for the model, the influence of both material and mechanical properties on hydrogel printability was initially evaluated. Two linear regression models were built: the first, based on material properties, used the concentrations of Gel-SH, HA-SH, and PEG-NB as input variables; the second, based on mechanical properties, included E, G', and G''. The results of these models are presented in Supporting Information S.4. At the end of this analysis, a comparison of the models indicated that material composition parameters exhibited a stronger correlation with the printability index than mechanical properties and were therefore selected as the primary inputs for subsequent modeling. To better explain the chemistry between hydrogels, masses were substituted with moles. In fact, only thiol groups of Gel-SH and HA-SH are involved in the crosslinking and not the total mass of samples. Equally, in PEG-NB, only terminal norbornene groups are involved; thus, the moles of reactive groups were determined using DoF calculated with ^{1}H-NMR. Once the model was established, it was compared to the previous mass-based model, showing no evident differences, as moles are proportional to mass; the mole-based approach is, however, chemically more accurate. The comparison scatter plot is presented in Supporting Information S.4. Following the establishment of the mole-based model, additional hydrogel formulations, including those previously excluded based on swelling tests, were included to increase the number of input data points. In fact, from a tissue engineering perspective, which aims to develop new in vitro functional tissues, only hydrogels that remain stable after swelling tests were considered, since a minimum requirement for supporting tissue growth is a suitable degradation rate, but a formulation can be printable even if it does not exhibit sufficient stability during swelling tests. For this reason, these additional formulations were also used into the dataset used for model development. Figure 16 shows the results of 3D printing for these formulations. For GelHA_0.24_30PEG, printing achieved good resolution and

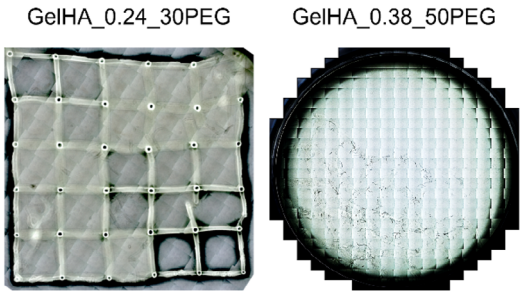

	Formation	SR	PA [%]	UF
GelHA_0.24_30PEG	Yes	0.87	99.7	1.04
GelHA_0.38_50PEG	Yes	--	--	--
GelHA_0.38_30PEG	No	--	--	--

FIGURE 16 | 3D printing of hydrogel formulations that were previously excluded based on swelling tests, which were included to increase the number of input data points for the model, along with their respective printing parameters.

maintained the intended shape, allowing the calculation of printing parameters. In the case of GelHA_0.38_50PEG, the hydrogel was printed, but the structure did not retain its shape during washing, while for GelHA_0.38_30PEG, printing did not occur. Since the models assume constant printing parameters, values of 0 were assigned for all three printing parameters in these two formulations.

Five different linear regression models were then developed to evaluate the printability index under varying assumptions: Model 1 used equal weights with molar concentrations of the materials as predictors, Model 2 applied empirically chosen weights based on the relative influence of each parameter on printing resolution, and Model 3 used regression-derived coefficients from standardized parameters. Models 4 and 5 were derived from Models 1 and 3, respectively, by including the DoC, calculated as the molar ratio between thiol groups and terminal groups of PEG-NB, as the input variable. The final dataset given in input is shown in Table 3.

To evaluate the performance of the predictive models, the predicted printability indexes were compared with the experimentally observed values obtained from 3D printing for both the original and newly added hydrogel formulations. In Supporting Information S.4., the comparison between observed and predicted values for each model is presented, enabling the assessment of model accuracy and consistency across different weighting schemes and the inclusion of the DoC. To further validate the models, their predictive capability was tested by providing as input three additional hydrogel formulations, for which theoretical printability indexes were calculated and subsequently compared with the experimentally determined ones (Table 4).

TABLE 3 | Final dataset of hydrogels given in input to models.

m Gel (mg)	m HA (mg)	m PEG (mg)	mol thiols	mol PEG-NB	DoC
18	2	70	0.0176	0.028	0.629
18	2	50	0.0176	0.020	0.880
18	2	30	0.0176	0.012	1.470
17	3	70	0.0163	0.028	0.582
17	3	50	0.0163	0.020	0.815
17	3	30	0.0163	0.012	1.358

In Figure 17, the 3D-printed structures of the three new hydrogel formulations are shown, together with their corresponding calculated printing parameters. All formulations were successfully printed, exhibiting good resolution and structural fidelity, with the second formulation showing particularly well-defined features. Following printing, printability indexes were calculated from the experimental printing parameters and compared with the theoretical values predicted by the five models, and the results of this comparison are reported in Supporting Information S.4.

Model 1, based on equal weights, showed acceptable agreement for the second formulation but tended to underestimate printability for the first and third formulations. Model 2, which applied empirically determined weights, exhibited the lowest predictive accuracy, with binary-like behavior (predicted values equal to 0 or 1), indicating an overfitting effect due to the limited dataset and the arbitrary weighting scheme. Model 3, which used regression-derived custom weights, provided a significantly improved correlation between predicted and observed data, demonstrating that data-driven weighting enhances the reliability of the printability prediction. The inclusion of the DoC in Models 4 and 5 further improved the correspondence with experimental values. Among all, Model 5 (custom weights + DoC) exhibited the best overall performance, with predicted printability indexes closely matching the observed ones for all three formulations.

To further visualize the predictive behavior of the models, scatter plots were generated for all models, while heatmaps and contour plots were additionally produced for Model 5, which demonstrated the best predictive performance. The scatter plots compare predicted versus experimentally obtained printability indexes, with the $y = x$ line representing perfect agreement; the closer the data points lie to this line, the more accurate the model (Figure 18). Heatmaps were used to illustrate predicted printability as a function of Gel-SH and PEG-NB concentrations

TABLE 4 | New formulations given to the model to validate its capability to predict their printability.

m Gel (mg)	m HA (mg)	m PEG (mg)	mol thiols	mol PEG-NB	DoC
17	3	60	0.0176	0.024	0.733
18.5	1.5	70	0.0157	0.028	0.561
16	4	55	0.0189	0.022	0.859

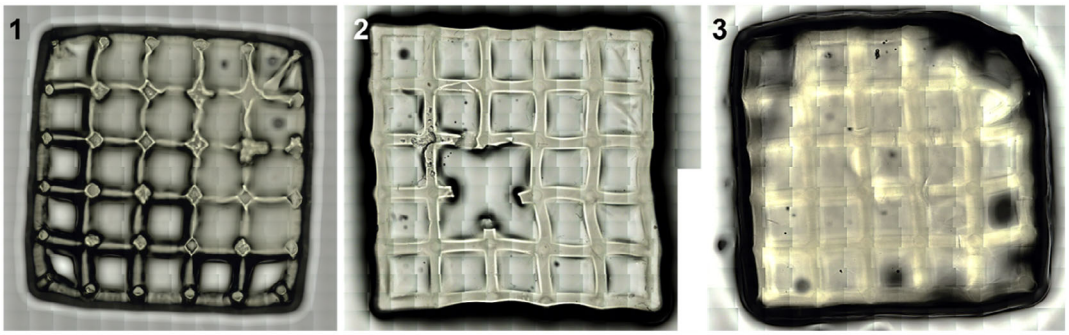

	m Gel [mg]	m HA [mg]	m PEG [mg]	Formation	SR	PA [%]	UF
1	17	3	60	Yes	1.08	86.4	0.92
2	18.5	1.5	70	Yes	1.06	76.1	0.94
3	16	4	55	Yes	1.06	96.4	0.93

FIGURE 17 | 3D printing of new hydrogel formulations developed to validate the predictive model.

for each fixed HA-SH value, where red regions indicate higher printability and white regions lower printability (Figure 19, first column). Complementary contour plots provide a gradient-based representation of the same data, facilitating the identification of optimal hydrogel compositions. These visualizations allow for an intuitive assessment of the effects of material composition and, when included, the DoC on hydrogel printability, highlighting regions where printing performance is predicted to be highest (Figure 19, second column).

To quantitatively evaluate differences between models and to find which is the best to predict printability, MAE and RMSE parameters were calculated for these formulations used as validation test, and the results are shown in Table 5. MAE and RMSE values equal to zero indicate perfect agreement between predicted and experimental values; therefore, lower values correspond to better predictive performance. As observed, Model 2 shows the poorest performance, with relatively high MAE and RMSE values. Model 1 exhibits slightly lower errors, but its predictive capability remains limited. In contrast, Model 3 yields error values below 0.2, indicating an acceptable level of prediction accuracy, and comparable results are observed for Model 4. The lowest errors are obtained for Model 5, consistent with previous observations, suggesting that the combination of data-driven weighting and DoC leads to improved predictive performance.

These results confirm that adding both chemically meaningful parameters (moles of reactive groups and DoC) and statistically optimized weighting factors leads to a more robust and accurate prediction of hydrogel printability. However, the predictive performance remains limited by the small size of the input dataset, which should be expanded to improve model generalization and reliability.

4 | Discussion

In this study, Gel and HA were both functionalized to introduce thiol groups, which are essential for crosslinking via UV-promoted thiol–ene radical addition [43, 48, 49]. By combining these biomaterials, six formulations were prepared via thiol–ene radical addition with PEG-NB, a mild reaction triggered by 405 nm UV light that occurs immediately upon exposure. This thiol–ene crosslinking approach has previously shown favorable results, as reported by Holmes et al., where Collagen-SH was crosslinked with PEG-NB using both LAP and I2959 [59]. The study demonstrated that I2959, when used at 365 nm, resulted in longer gelation times, whereas LAP was the most efficient initiator, supporting our choice for this system. Swelling tests were conducted at three different pH values to identify the most suitable formulations for tissue engineering applications. Formulations with lower PEG content showed poor performance, fully degrading by day 7 at all tested pH levels. Similarly, GelHA_0.38_50PEG was unstable under neutral conditions, leading to its exclusion along with the 30PEG formulations. In contrast, higher PEG content hydrogels, GelHA_0.24_70PEG and GelHA_0.38_70PEG, demonstrated greater stability and consistent swelling across pH levels, while GelHA_0.24_50PEG was also included for its favorable swelling at pH 7.4, highlighting the influence of both PEG content and material composition on hydrogel behavior [51]. Hydrogel formation for the selected formulations was confirmed by ^{1}H-NMR analysis, showing peak reductions of 68.3%, 86.9%, and 89.9% for GelHA_0.24_70PEG, GelHA_0.24_50PEG, and GelHA_0.38_70PEG, respectively. Amplitude sweep test was performed to compare hydrogel formulations from a rheological perspective, examining G' in relation to the concentrations of Gel-SH, HA-SH, and PEG-NB. All hydrogels displayed a similar LVR up to ~1% strain, after which G'' became strain-dependent, while G' remained stable up to 8–10% strain. Formulations with higher PEG content exhibited increased G' values, whereas reducing PEG led to higher flow strain. These results suggest that crosslink density, driven mainly by PEG-NB concentration rather than biomaterial content, dominates hydrogel viscoelasticity: higher PEG-NB increases both G' and G'' while reducing deformability, in agreement with a previous study in which greater PEG-based crosslinking enhances hydrogel stiffness and storage modulus [60]. However, compression tests revealed that HA content, rather than PEG concentration, had a stronger influence on hydrogel mechanical strength. This finding is consistent with our previous work, where enzymatically crosslinked hydrogels exhibited enhanced

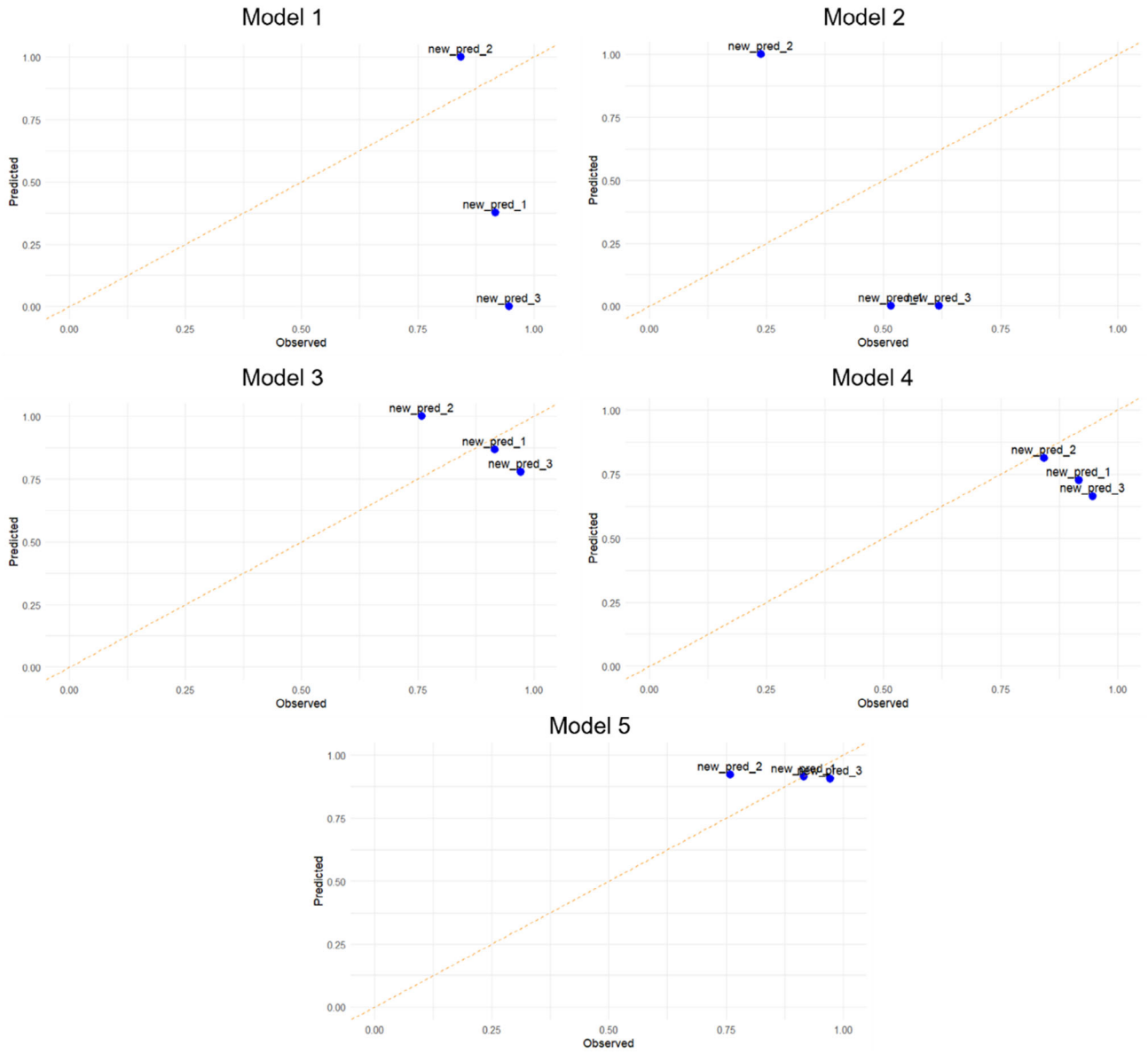

FIGURE 18 | Scatter plots comparing the predicted and experimental printability indexes for the different models. The orange dashed line represents $y = x$, corresponding to a perfect agreement between predicted and observed values. Blue points indicate the printability index of each hydrogel formulation; the closer they lie to the orange line, the more accurately the model predicts the actual 3D printing behavior.

mechanical properties with increasing HA content [37]. To assess cell survival and spreading potential within hydrogels despite their low porosity and high stiffness, hBM-MSCs were seeded using two approaches: encapsulated within the hydrogel prior to crosslinking or seeded on the hydrogel surface after crosslinking. Metabolic activity showed a slight increase in the encapsulated samples, while surface-seeded samples exhibited a more pronounced increase over time. Live-Dead staining confirmed high cell viability in all conditions, with only a few dead cells observed across time points. Notably, differences in cell morphology were detected between the two seeding strategies. In surface-seeded hydrogels, cells initially formed aggregates and exhibited elongation during the early days of culture, subsequently migrating into the hydrogel bulk. In contrast, encapsulated cells remained rounded and uniformly distributed throughout the hydrogel. Quantitative roundness analysis following Phalloidin and DAPI staining confirmed these observations and additionally revealed that cells in hydrogels with higher Gel content, particularly GelHA_0.24_50PEG, tended to adopt a more elongated morphology, both for encapsulated and surface-seeded populations. Stiffness is known to influence cell adhesion and spreading, with intermediate stiffness generally promoting optimal cellular behavior; therefore, the target application of the construct should guide the selection of hydrogel mechanical properties [61, 62]. In this study, hydrogels with enhanced mechanical strength were developed to improve printing resolution and enable the fabrication of complex structures. Because softer hydrogels, characterized by a lower crosslinking density, tend to poorly retain their shape after printing, particularly under swelling conditions, we instead designed stiffer hydrogels intended for post-printing cell seeding.

Hydrogel 3D printing was carried out using stereolithography, which enables crosslinking through UV light exposure. To assess printing fidelity, an STL mesh model with a fine strand diameter

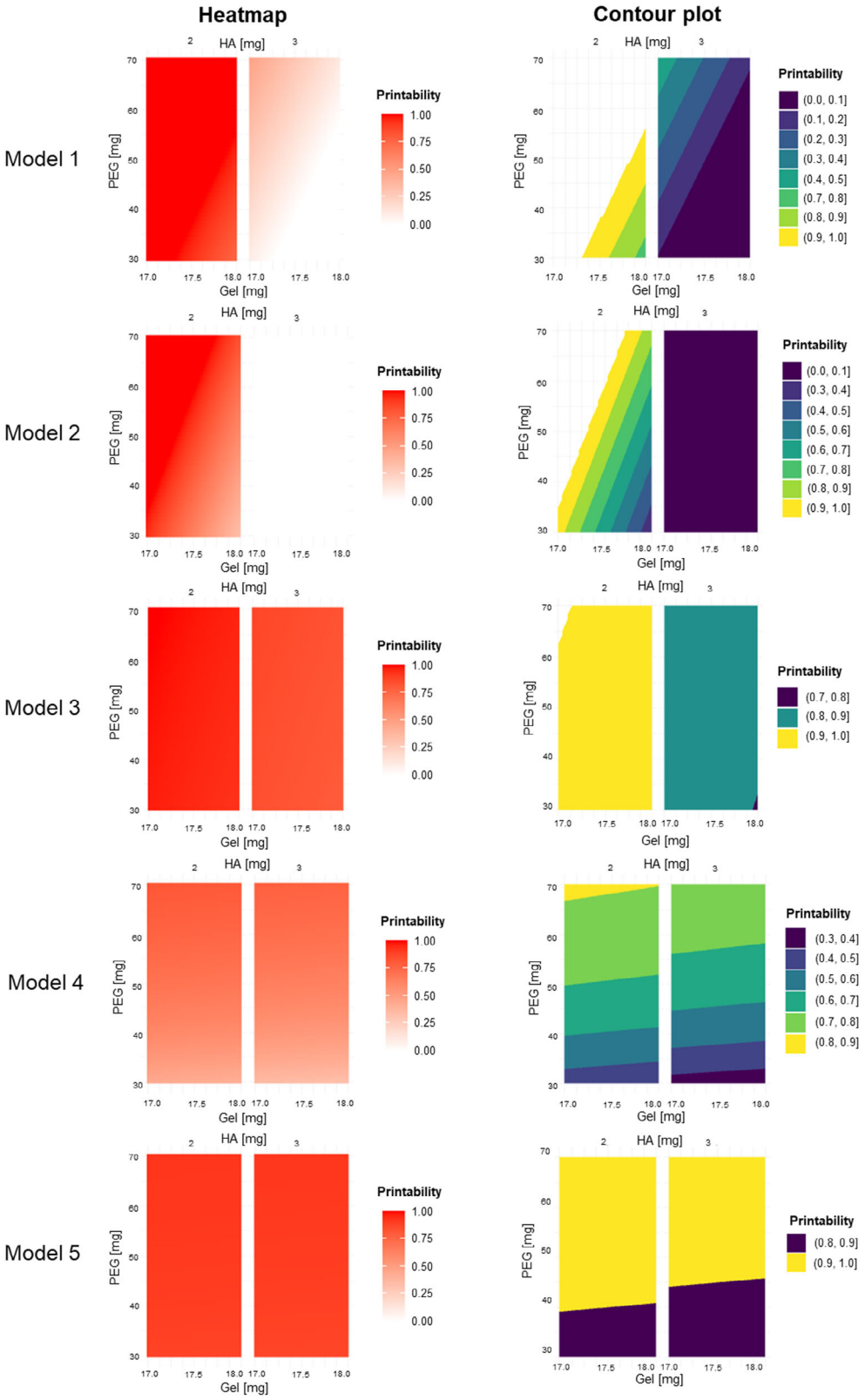

FIGURE 19 | Heatmaps and contour plots of results.

of 0.4 mm was designed. All formulations demonstrated excellent printability and accurately reproduced the mesh architecture, outperforming structures produced by extrusion-based methods. For comparison, previous studies reported PEG–heparin scaffolds fabricated by extrusion with a similar mesh design, but with lower resolution and fidelity, highlighting the superior precision of stereolithography [63]. In addition, a previous work highlighted that an ongoing challenge in biofabrication is the 3D printing of hydrogels with lower stiffness, as most used hydrogels exhibit G' above 5000 Pa, which can negatively affect cells. In

TABLE 5 | MAE and RMSE values obtained for validation formulations of models.

Model	MAE	RMSE
1	0.5474	0.6354
2	0.6326	0.6405
3	0.1615	0.1810
4	0.1681	0.1979
5	0.0773	0.1011

that study, a Gel-SH and PEG-NB hydrogel system was shown to provide optimal printability while maintaining a soft matrix [64]. Building upon this, we included HA, which plays a crucial role in supporting cell viability due to its swelling capacity and water-retention properties. SEM analysis showed a uniform, compact hydrogel structure with minimal porosity. Therefore, the small functional groups used to modify Gel and HA (γ-thiobutyrolactone and cysteamine) likely promote the formation of a dense network via thiol–ene crosslinking. Troncoso-Afonso et al. [65] reported similar findings with thiol–ene Gel-NB and Gel-SH hydrogels, which exhibited a distinct porous structure characterized by small, dense pores. In comparison, hydrogels formulated with alginate or carboxymethylcellulose displayed larger, less compact pores. These results suggest that the observed dense network is a combined effect of the presence of Gel and the thiol–ene crosslinking strategy, as the crosslinking method alone would produce larger pores when applied to other polymer systems.

Following these results, a preliminary predictive model was developed to estimate the printability of thiol–ene crosslinked hydrogels and to assess whether computational prediction could reliably evaluate their printing behavior. This approach is particularly relevant in the context of AI-guided material design, which can optimize material parameters by predicting them from final properties. By analyzing large amounts of experimental and computational data, ML algorithms can extract underlying relationships and construct models capturing the complex interplay between material composition, structure, and properties [30, 66, 67]. Unfortunately, the application of machine learning in biomaterials design is limited by several factors, including the availability of high-quality data required to train the models [68]. Although the dataset available in this study was small, which could lead to issues such as data imbalance and over- or underfitting [69], the modeling algorithm was specifically designed to handle limited datasets. Additionally, hydrogel formulations that had been previously excluded based on swelling tests were included as input to expand the dataset. Nevertheless, further increasing the number of data points would likely enhance the predictive performance of the models. After identifying the most relevant parameters describing hydrogel printability, five different models were developed, varying the weighting assigned to each calculated printing parameter and adding the DoC as an additional input where appropriate. Linear regression was selected due to the limited size of the available dataset, which restricts the robustness of more complex nonlinear models and increases the risk of overfitting. In this context, a linear approach provides a more stable and interpretable framework for analyzing the relationship between input parameters and printability score. These regression-based models were subsequently compared to determine which approach best captures the printability behavior of the formulations within this limited dataset. The formulation of the printability score involves a degree of subjectivity in the assignment of weighting coefficients. However, the object of this study was not to assume a predefined weighting scheme, but to identify the most suitable printability model by systematically varying both the input parameters and their associated weights. Specifically, different weighting strategies were explored, including equal weights, empirically assigned weights based on the perceived importance of each parameter, and data-driven weights derived from regression analysis. The resulting models were then compared based on their ability to reflect experimental observations and discriminate between printing outcomes. Within this framework, sensitivity to the weighting scheme is an expected and integral aspect of the model selection process, rather than a limitation.

To validate the models, new hydrogel formulations were developed and 3D printed, and their experimentally measured printability indexes were compared with the predicted values. Model 2 performed the worst (MAE = 0.6326), as it relied on empirically assigned, human-defined weights. In contrast, Model 5 showed the best performance (MAE = 0.0773), accurately capturing printability behavior by integrating data-driven weights with the degree of conversion (DoC). These results highlight the importance of combining chemically meaningful parameters with data-driven approaches to achieve optimal predictive performance. Furthermore, ML models trained on appropriate chemical descriptors can provide reliable predictions even when only small datasets are available. This work represents a proof of concept, as MAE and RMSE evaluated on a limited dataset require cautious interpretation of generalizability. In this "smart data" framework, these metrics are used for model comparison rather than universal validation, with the low RMSE–MAE gap indicating locally robust predictions enabled by mechanistic descriptors such as DoC.

Regression is a widely used method in ML and has demonstrated good reliability. In Xu et al., Bayesian regression was applied using experimental parameters as input to predict the behavior of unknown data points, with the resulting model aligning with experimentally observed property trends, reflecting the practical utility of the approach [70]. In another study, regression-based machine learning methods were used to model the relationship between synthesis conditions and hydrogel swelling behavior, demonstrating that the chosen model could predict discrete swelling states and generate swelling curves [71]. Despite these examples, the application of regression-based models in light-initiated 3D printing remains limited. Therefore, the approach presented in this study, even with a small dataset, provides a valuable strategy to explore the link between ML and 3D printing of hydrogels.

5 | Limits and Perspectives

A key limitation of this study is the relatively small dataset used for model development, which increases the risk of overfitting

and limits the generalizability of the results. For this reason, the proposed models should be considered as a proof of concept rather than fully predictive tools. This work is intended as an exploratory analysis to identify relevant trends between printing parameters and printability rather than to provide a universal predictive framework. Future studies based on larger datasets will be required to validate and extend these findings. Additionally, future studies with larger datasets may explore methods such as support vector regression or Gaussian process regression to better capture nonlinear relationships. Another limitation is that the current model does not include metrics related to the biological activity of the hydrogels. Due to the limited number of input formulations, adding biological parameters would likely increase the risk of overfitting; therefore, the model was deliberately simplified to focus on printing-related properties. Future studies with larger datasets could integrate biological descriptors to enable the simultaneous prediction of printability and biological performance. For example, an extended version of the model could include a biological spreading score to quantify the relationship between printing resolution and the ability of hydrogels to support cell migration.

6 | Conclusions

This study focused on the optimization of Gel-SH and HA-SH hydrogels for high-resolution stereolithographic 3D printing. Exploiting thiol–ene photocrosslinking, we generated constructs with superior structural fidelity compared to conventional extrusion-based methods, while maintaining a biocompatible environment for hBM-MSCs. Selected formulations showed suitable mechanical properties, and biological tests confirmed their ability to support cell adhesion and proliferation. A key contribution is the development of an ML-based predictive framework effective even with limited data. By integrating mechanistic descriptors such as DoC and functional group ratios, the model achieved improved predictive performance, highlighting the advantage of combining chemical insight with data-driven approaches. This work represents a proof of concept, as metrics such as MAE and RMSE were evaluated on a small dataset and should be interpreted cautiously. In this context, these metrics are primarily used for methodological comparison rather than universal validation, with the low RMSE-MAE gap suggesting locally robust predictions driven by mechanistic descriptors. The high crosslinking density ensured structural stability but may limit cell migration, representing a key trade-off for future work. Further developments will focus on integrating biological descriptors, defining a biological spread score, and introducing degradable crosslinkers. In conclusion, this ML-guided approach accelerates biomaterial optimization by reducing experimental effort while providing a robust proof of concept for the design of high-precision, customizable ECM-mimicking scaffolds for tissue engineering.

Author Contributions

Maddalena Bracchi: writing – original draft, methodology, investigation, formal analysis, data curation. **Francesco Nicotra**: writing – review & editing, funding acquisition. **Laura Russo**: writing – review & editing, supervision, project administration, funding acquisition.

Acknowledgments

The authors received financial support from PNRR—AdvaNced Technologies for Human-centrEd Medicine (ANTHEM)—PNC0000003—Finanziato dallUnione Europea—NextGenerationEU—Avviso 931/2022—Spoke 2; CIG: BB1674602E, CUP: B53C22006670001; Ministero della Salute, RF-2021–12371959. Tackling immunomodulatory properties of stromal cells to improve therapeutic strategies in lung cancer. MUR PRIN 2022, 2022MY7AZT Dynamic multifunctional hydrogels for glioblastoma therapy (DINGO).

Open access publishing facilitated by Universita degli Studi di Milano-Bicocca, as part of the Wiley - CRUI-CARE agreement.

Funding

This study was supported by Ministero dell'Università e della Ricerca (B53C2200667000).

Conflicts of Interest

The authors declare no conflicts of interest.

Data Availability Statement

The data that support the findings are publicly available in Zenodo at DOI: https://doi.org/10.5281/zenodo.20323049 and in the Supporting Information of this article.

References

1. S. Li, X. Dan, H. Chen, et al., "Developing Fibrin-Based Biomaterials/Scaffolds in Tissue Engineering," *Bioactive Materials* 40 (2024): 597–623, https://doi.org/10.1016/j.bioactmat.2024.08.006.

2. N. Kasoju and A. Sunilkumar, "Convergence of Tissue Engineering and Sustainable Development Goals," *Biotechnology for Sustainable Materials* 1, no. 1 (2024): 20, https://doi.org/10.1186/s44316-024-00021-y.

3. V. D. L. Putra, K. A. Kilian, and M. L. Knothe Tate, "Biomechanical, Biophysical and Biochemical Modulators of Cytoskeletal Remodelling and Emergent Stem Cell Lineage Commitment," *Communications Biology* 6, no. 1 (2023): 75, https://doi.org/10.1038/s42003-022-04320-w.

4. K. Dzobo and C. Dandara, "The Extracellular Matrix: Its Composition, Function, Remodeling, and Role in Tumorigenesis," *Biomimetics* 8, no. 2 (2023): 146, https://doi.org/10.3390/biomimetics8020146.

5. A. Berdiaki, M. Neagu, P. Tzanakakis, I. Spyridaki, S. Pérez, and D. Nikitovic, "Extracellular Matrix Components and Mechanosensing Pathways in Health and Disease," *Biomolecules* 14, no. 9 (2024): 1186, https://doi.org/10.3390/biom14091186.

6. P. Kesharwani, A. Alexander, R. Shukla, et al., "Tissue Regeneration Properties of Hydrogels Derived from Biological Macromolecules: A Review," *International Journal of Biological Macromolecules* 271 (2024): 132280, https://doi.org/10.1016/j.ijbiomac.2024.132280.

7. S. Romano, S. Yazdanpanah, O. Petillo, et al., "Sustainable Hydrogels for Medical Applications: Biotechnological Innovations Supporting One Health," *Gels* 11, no. 7 (2025): 559, https://doi.org/10.3390/gels11070559.

8. T.-C. Ho, C.-C. Chang, H.-P. Chan, et al., "Hydrogels: Properties and Applications in Biomedicine," *Molecules* 27, no. 9 (2022): 2902, https://doi.org/10.3390/molecules27092902.

9. X. B. Chen, A. Fazel Anvari-Yazdi, X. Duan, et al., "Biomaterials / Bioinks and Extrusion Bioprinting," *Bioactive Materials* 28 (2023): 511–536, https://doi.org/10.1016/j.bioactmat.2023.06.006.

10. A. S. Priya, R. Premanand, I. Ragupathi, et al., "Comprehensive Review of Hydrogel Synthesis, Characterization, and Emerging

Applications," *Journal of Composites Science* 8, no. 11 (2024): 457, https://doi.org/10.3390/jcs8110457.

11. M. Mirshafiei, H. Rashedi, F. Yazdian, A. Rahdar, and F. Baino, "Advancements in Tissue and Organ 3D Bioprinting: Current Techniques, Applications, and Future Perspectives," *Materials & Design* 240 (2024): 112853, https://doi.org/10.1016/j.matdes.2024.112853.

12. M. Camacho-Cardenosa, V. Pulido-Escribano, G. Estrella-Guisado, et al., "Bioprinted Hydrogels as Vehicles for the Application of Extracellular Vesicles in Regenerative Medicine," *Gels* 11, no. 3 (2025): 191, https://doi.org/10.3390/gels11030191.

13. R. V. Barrulas and M. C. Corvo, "Rheology in Product Development: An Insight into 3D Printing of Hydrogels and Aerogels," *Gels* 9, no. 12 (2023): 986, https://doi.org/10.3390/gels9120986

14. Y. Jeon, M. Kim, and K. H. Song, "Development of Hydrogels Fabricated via Stereolithography for Bioengineering Applications," *Polymers* 17, no. 6 (2025): 765, https://doi.org/10.3390/polym17060765.

15. C. Alparslan and Ş. Bayraktar, "Advances in Digital Light Processing (DLP) Bioprinting: A Review of Biomaterials and Its Applications, Innovations, Challenges, and Future Perspectives," *Polymers* 17, no. 9 (2025): 1287, https://doi.org/10.3390/polym17091287.

16. L. Guida, M. Cavallaro, and M. Levi, "Advancements in High-Resolution 3D Bioprinting: Exploring Technological Trends, Bioinks and Achieved Resolutions," *Bioprinting* 44 (2024): e00376, https://doi.org/10.1016/j.bprint.2024.e00376.

17. F. Damiri, A. Fatimi, Y. Liu, et al., "Recent Advances in 3D Bioprinted Polysaccharide Hydrogels for Biomedical Applications: A Comprehensive Review," *Carbohydrate Polymers* 348 (2025): 122845, https://doi.org/10.1016/j.carbpol.2024.122845.

18. A. P. Dhand, M. D. Davidson, and J. A. Burdick, "Lithography-Based 3D Printing of Hydrogels," *Nature Reviews Bioengineering* 3, no. 2 (2025): 108–125, https://doi.org/10.1038/s44222-024-00251-9.

19. A. Afridi, A. Al Rashid, and M. Koç, "Recent Advances in the Development of Stereolithography-Based Additive Manufacturing Processes: A Review of Applications and Challenges," *Bioprinting* 43 (2024): e00360, https://doi.org/10.1016/j.bprint.2024.e00360.

20. H. Omidian and K. Mfoafo, "Three-Dimensional Printing Strategies for Enhanced Hydrogel Applications,"*Gels* 10, no. 4 (2024): 220, https://doi.org/10.3390/gels10040220.

21. K. Ghosal, S. K. Bhattacharyya, V. Mishra, and H. Zuilhof, "Click Chemistry for Biofunctional Polymers: From Observing to Steering Cell Behavior," *Chemical Reviews* 124, no. 23 (2024): 13216–13300, https://doi.org/10.1021/acs.chemrev.4c00251.

22. Z. Xu and K. M. Bratlie, "Click Chemistry and Material Selection for, *In Situ*, Fabrication of Hydrogels in Tissue Engineering Applications," *ACS Biomaterials Science & Engineering* 4, no. 7 (2018): 2276–2291, https://doi.org/10.1021/acsbiomaterials.8b00230.

23. F. Cadamuro, F. Nicotra, and L. Russo, "3D Printed Tissue Models: From Hydrogels to Biomedical Applications," *Journal of Controlled Release* 354 (2023): 726–745, https://doi.org/10.1016/j.jconrel.2023.01.048.

24. A. P. Malafaia, R. Sobreiro-Almeida, J. M. M. Rodrigues, and J. F. Mano, "Thiol-ene Click Chemistry: Enabling 3D Printing of Natural-Based Inks for Biomedical Applications," *Biomaterials Advances* 167 (2025): 214105, https://doi.org/10.1016/j.bioadv.2024.214105.

25. R. Laurano, M. Boffito, C. Cassino, et al., "Thiol-Ene Photo-Click Hydrogels with Tunable Mechanical Properties Resulting from the Exposure of Different -Ene Moieties through a Green Chemistry," *Materials* 16, no. 5 (2023): 2024, https://doi.org/10.3390/ma16052024.

26. L. K. Jang, J. T. Ahlquist, C. Ye, et al., "Rapid Curing Dynamics of PEG-Thiol-ene Resins Allow Facile 3D Bioprinting and in-Air Cell-Laden Microgel Fabrication," *Biomedical Materials* 20, no. 1 (2025): 015009, https://doi.org/10.1088/1748-605X/ad8540.

27. C. Lin, C. S. Ki, and H. Shih, "Thiol–norbornene Photoclick Hydrogels for Tissue Engineering Applications," *Journal of Applied Polymer Science* 132, no. 8 (2015), https://doi.org/10.1002/app.41563.

28. I. P. Malashin, D. Martysyuk, V. Nelyub, A. Borodulin, A. Gantimurov, and V. Tynchenko, "Deep Learning for Property Prediction of Natural Fiber Polymer Composites," *Scientific Reports* 15, no. 1 (2025): 27837, https://doi.org/10.1038/s41598-025-10841-1.

29. G. D. Goh, S. L. Sing, and W. Y. Yeong, "A Review on Machine Learning in 3D Printing: Applications, Potential, and Challenges," *Artificial Intelligence Review* 54, no. 1 (2021): 63–94, https://doi.org/10.1007/s10462-020-09876-9.

30. Y. Jin, M. Hu, P. Zhao, et al., "AI-Guided Biomaterials and Biofabrication Strategies for Enhanced Tumor Extracellular Matrix Mimicry," *Cell Biomaterials* 2 (2026): 100188, https://doi.org/10.1016/j.celbio.2025.100188.

31. J. Lee, S. J. Oh, S. H. An, W.-D. Kim, and S.-H. Kim, "Machine Learning-Based Design Strategy for 3D Printable Bioink: Elastic Modulus and Yield Stress Determine Printability," *Biofabrication* 12, no. 3 (2020): 035018, https://doi.org/10.1088/1758-5090/ab8707.

32. R. Sarah, K. Schimmelpfennig, R. Rohauer, C. L. Lewis, S. M. Limon, and A. Habib, "Characterization and Machine Learning-Driven Property Prediction of a Novel Hybrid Hydrogel Bioink Considering Extrusion-Based 3D Bioprinting," *Gels* 11, no. 1 (2025) 45, https://doi.org/10.3390/gels11010045.

33. D. Gogoi, M. Kumar, and J. Singh, "A Comprehensive Review on Hydrogel-Based Bio-Ink Development for Tissue Engineering Scaffolds Using 3D Printing," *Annals of 3D Printed Medicine* 15 (2024): 100159, https://doi.org/10.1016/j.stlm.2024.100159.

34. Y. Dai, P. Wang, A. Mishra, et al., "3D Bioprinting and Artificial Intelligence-Assisted Biofabrication of Personalized Oral Soft Tissue Constructs," *Advanced Healthcare Materials* 14, no. 13 (2025), https://doi.org/10.1002/adhm.202402727.

35. K. Ruberu, M. Senadeera, S. Rana, et al., "Coupling Machine Learning with 3D Bioprinting to Fast Track Optimisation of Extrusion Printing," *Applied Materials Today* 22 (2021): 100914, https://doi.org/10.1016/j.apmt.2020.100914.

36. T. X. Morrison and W. M. Gramlich, "Tunable, Thiol-ene, Interpenetrating Network Hydrogels of Norbornene-Modified Carboxymethyl Cellulose and Cellulose Nanofibrils," *Carbohydrate Polymers* 319 (2023): 121173, https://doi.org/10.1016/j.carbpol.2023.121173.

37. M. Bracchi, F. Nicotra, and L. Russo, "3D Bioprintable Hydrogels via Enzymatic Crosslinking of Hyaluronic Acid and Phenol-Functionalized Gelatin to Mimic Extracellular (ECM) Network," *Carbohydrate Polymer Technologies and Applications* 11 (2025): 100928, https://doi.org/10.1016/j.carpta.2025.100928.

38. K. Su and C. Wang, "Recent Advances in the use of Gelatin in Biomedical Research," *Biotechnology Letters* 37, no. 11 (2015): 2139–2145, https://doi.org/10.1007/s10529-015-1907-0.

39. S. Sampaolesi, F. Nicotra, and L. Russo, "Glycans in Nanomedicine, Impact and Perspectives," *Future Medicinal Chemistry* 11, no. 1 (2019): 43–60, https://doi.org/10.4155/fmc-2018-0368.

40. M. Bracchi, F. Nicotra, and L. Russo, "Glyco-Functionalization of ECM Mimics, Influence in Morphology and Cell Behaviour Authors," *RSC Chemical Biology* 6 (2025): 1893–1908, https://doi.org/10.1039/D5CB00185D.

41. F. Barbugian, D. Salerno, E. Ballarini, et al., "Bioresponsive Hyaluronic Acid-Based Hydrogel Inhibits Matrix Metalloproteinase-2 in Glioblastoma Microenvironment," *ChemMedChem* 20, no. 15 (2025), https://doi.org/10.1002/cmdc.202401040.

42. K. Jin, A. Xing, and M. Bilal, "Plane Morphometric Analysis of Particles Using an Automatic Image Analysis System: A Case Study of

the Xinmo Landslide," *Granular Matter* 26, no. 1 (2024): 4, https://doi.org/10.1007/s10035-023-01375-2.

43. A. Pariskar, P. K. Sharma, U. S. Murty, and S. Banerjee, "Effect of Tartrazine as Photoabsorber for Improved Printing Resolution of 3D Printed Ghost Tablets: Non-Erodible Inert Matrices," *Journal of Pharmaceutical Sciences* 112, no. 4 (2023): 1020–1031, https://doi.org/10.1016/j.xphs.2022.11.014.

44. A. Schwab, R. Levato, M. D'Este, S. Piluso, D. Eglin, and J. Malda, "Printability and Shape Fidelity of Bioinks in 3D Bioprinting," *Chemical Reviews* 120, no. 19 (2020): 11028–11055, https://doi.org/10.1021/acs.chemrev.0c00084.

45. D. Ribezzi, R. Pinos, L. Bonetti, et al., "Design of a Novel Bioink Suitable for the 3D Printing of Lymphoid Cells," *Frontiers in Biomaterials Science* 2 (2023), https://doi.org/10.3389/fbiom.2023.1081065.

46. M. D. Giuseppe, N. Law, B. Webb, et al., "Mechanical Behaviour of Alginate-Gelatin Hydrogels for 3D Bioprinting," *Journal of the Mechanical Behavior of Biomedical Materials* 79 (2018): 150–157, https://doi.org/10.1016/j.jmbbm.2017.12.018.

47. N. Soltan, L. Ning, F. Mohabatpour, P. Papagerakis, and X. Chen, "Printability and Cell Viability in Bioprinting Alginate Dialdehyde-Gelatin Scaffolds," *ACS Biomaterials Science & Engineering* 5, no. 6 (2019): 2976–2987, https://doi.org/10.1021/acsbiomaterials.9b00167.

48. M. Bertuola, B. Aráoz, U. Gilabert, et al., "Gelatin–alginate–hyaluronic Acid Inks for 3D Printing: Effects of Bioglass Addition on Printability, Rheology and Scaffold Tensile Modulus," *Journal of Materials Science* 56, no. 27 (2021): 15327–15343, https://doi.org/10.1007/s10853-021-06250-0.

49. Posit Team, "RStudio: Integrated Development Environment for R," Posit Software, PBC, 2025, http://www.posit.co/.

50. J. Franklin, "The Elements of Statistical Learning: Data Mining, Inference and Prediction," *The Mathematical Intelligencer* 27, no. 2 (2005): 83–85, https://doi.org/10.1007/BF02985802.

51. T. O. Hodson, "Root-Mean-Square Error (RMSE) or Mean Absolute Error (MAE): When to use Them or Not," *Geoscientific Model Development* 15, no. 14 (2022): 5481–5487, https://doi.org/10.5194/gmd-15-5481-2022.

52. S. Lee and D. K. Lee, "What Is the Proper Way to Apply the Multiple Comparison Test?," *Korean Journal of Anesthesiology* 71, no. 5 (2018): 353–360, https://doi.org/10.4097/kja.d.18.00242.

53. C. E. Agbangba, E. Sacla Aide, H. Honfo, and R. Glèlè Kakai, "On the use of Post-Hoc Tests in Environmental and Biological Sciences: A Critical Review," *Heliyon* 10, no. 3 (2024): e25131, https://doi.org/10.1016/j.heliyon.2024.e25131.

54. T. Göckler, S. Haase, X. Kempter, et al., "Tuning Superfast Curing Thiol-Norbornene-Functionalized Gelatin Hydrogels for 3D Bioprinting," *Advanced Healthcare Materials* 10, no. 14 (2021), https://doi.org/10.1002/adhm.202100206.

55. L. Russo, A. Sgambato, R. Visone, et al., "Gelatin Hydrogels via Thiol-ene Chemistry," *Monatshefte für Chemie - Chemical Monthly* 147, no. 3 (2016): 587–592, https://doi.org/10.1007/s00706-015-1614-5.

56. I. Youm, V. Agrahari, J. B. Murowchick, and B.-B. C. Youan, "Uptake and Cytotoxicity of Docetaxel-Loaded Hyaluronic Acid-Grafted Oily Core Nanocapsules in MDA-MB. 231 Cancer Cells," *Pharmaceutical Research* 31, no. 9 (2014): 2439–2452, https://doi.org/10.1007/s11095-014-1339-x.

57. K. Raghupathi and S. Thayumanavan, "Nano-Armoring of Enzymes," in *Methods in Enzymology* (Elsevier, 2017), 381–411, https://doi.org/10.1016/bs.mie.2017.01.007.

58. N. Toncheva-Moncheva, M. Dangalov, N. G. Vassilev, and C. P. Novakov, "Thiol–ene Coupling Reaction Achievement and Monitoring by, *In Situ*, UV Irradiation NMR Spectroscopy," *RSC Advances* 10, no. 42 (2020): 25214–25222, https://doi.org/10.1039/D0RA03902K.

59. R. Holmes, X.-B. Yang, A. Dunne, L. Florea, D. Wood, and G. Tronci, "Thiol-Ene Photo-Click Collagen-PEG Hydrogels: Impact of Water-Soluble Photoinitiators on Cell Viability, Gelation Kinetics and Rheological Properties," *Polymers* 9, no. 6 (2017): 226, https://doi.org/10.3390/polym9060226.

60. C.-W. Chu, W. J. Cheng, B. Y. Wen, et al., "Preparation and Rheological Evaluation of Thiol–Maleimide/Thiol–Thiol Double Self-Crosslinking Hyaluronic Acid-Based Hydrogels as Dermal Fillers for Aesthetic Medicine," *Gels* 10, no. 12 (2024): 776, https://doi.org/10.3390/gels10120776.

61. P. Yang, G. Boer, F. Snow, et al., "Test and Tune: Evaluating, Adjusting and Optimising the Stiffness of Hydrogels to Influence Cell Fate," *Chemical Engineering Journal* 505 (2025): 159295, https://doi.org/10.1016/j.cej.2025.159295.

62. K. C. M. L. Elvitigala, L. Mohan, W. Mubarok, and S. Sakai, "Phototuning of Hyaluronic-Acid-Based Hydrogel Properties to Control Network Formation in Human Vascular Endothelial Cells," *Advanced Healthcare Materials* 13, no. 17 (2024), https://doi.org/10.1002/adhm.202303787.

63. E. Pérez Del Río, S. Rey-Vinolas, Fão Santos, et al., "3D Printing as a Strategy to Scale-Up Biohybrid Hydrogels for T Cell Manufacture," *ACS Applied Materials & Interfaces* 16, no. 38 (2024): 50139–50146, https://doi.org/10.1021/acsami.4c06183.

64. V. T. Duong and C. Lin, "Digital Light Processing 3D Bioprinting of Gelatin-Norbornene Hydrogel for Enhanced Vascularization," *Macromolecular Bioscience* 23, no. 12 (2023), https://doi.org/10.1002/mabi.202300213.

65. L. Troncoso-Afonso, Y. M. Henríquez-Banegas, G. A. Vinnacombe-Willson, et al., "Using Thiol–ene Click Chemistry to Engineer 3D Printed Plasmonic Hydrogel Scaffolds for SERS Biosensing," *Biomaterials Science* 13, no. 11 (2025): 2936–2950, https://doi.org/10.1039/D4BM01529K.

66. S. M. McDonald, E. K. Augustine, Q. Lanners, C. Rudin, L. Catherine Brinson, and M. L. Becker, "Applied Machine Learning as a Driver for Polymeric Biomaterials Design," *Nature Communications* 14, no. 1 (2023): 4838, https://doi.org/10.1038/s41467-023-40459-8.

67. F. Cadamuro, M. Piazzoni, E. Gamba, et al., "Artificial Intelligence Tool for Prediction of ECM Mimics Hydrogel Formulations via Click Chemistry," *Biomaterials Advances* 175 (2025): 214323, https://doi.org/10.1016/j.bioadv.2025.214323.

68. M. J. Tamasi, R. A. Patel, C. H. Borca, et al., "Machine Learning on a Robotic Platform for the Design of Polymer–Protein Hybrids," *Advanced Materials* 34, no. 30 (2022), https://doi.org/10.1002/adma.202201809.

69. P. Xu, X. Ji, M. Li, and W. Lu, "Small Data Machine Learning in Materials Science," *npj Computational Materials* 9, no. 1 (2023): 42, https://doi.org/10.1038/s41524-023-01000-z.

70. S. Xu, X. Chen, S. Wang, Z. Chen, P. Pan, and Q. Huang, "Integrating Machine Learning for the Optimization of Polyacrylamide/Alginate Hydrogel," *Regenerative Biomaterials* 11 (2024), https://doi.org/10.1093/rb/rbae109.

71. Y. Wang, T. Wallmersperger, and A. Ehrenhofer, "Prediction of Hydrogel Swelling States Using Machine Learning Methods," *Engineering Reports* 6, no. 11 (2024), https://doi.org/10.1002/eng2.12893.

Supporting Information

Additional supporting information can be found online in the Supporting Information section.